

Authigenic carbonate burial in the Late Devonian–Early Mississippian Bakken Formation (Williston Basin, USA)

BEN DAVIS BARNES*† , JON M. HUSSON*‡ and SHANAN E. PETERS*

*Department of Geoscience, University of Wisconsin–Madison, 1215 W. Dayton Street, Madison, WI 53706, USA (E-mail: bdavisbarnes@psu.edu)

†Department of Geosciences, The Pennsylvania State University, Deike Building, University Park, PA 16802, USA

‡School of Earth and Ocean Sciences, University of Victoria, 2800 Finnerty Road, Victoria, BC V8W 2Y2, Canada

Associate Editor – Nicholas Tosca

ABSTRACT

Late Devonian (Famennian) marine successions globally are typified by organic-rich black shales deposited in anoxic and euxinic waters and the cessation of shelf carbonate sedimentation. This global ‘carbonate crisis’, known as the Hangenberg Event, coincides with a major extinction of reef-building metazoans and perturbations to the global carbon cycle, evidenced by positive carbon-isotope excursions of up to 4‰. It has been suggested that authigenic carbonate, formed as cements in sedimentary pore spaces during early burial diagenesis, is a significant mass fraction of the total global carbon burial flux, particularly during periods of low oxygen concentration. Because some authigenic carbonate could have originated from remineralization of organic carbon in sediments, it is possible for this reservoir to be isotopically depleted and thereby drive changes in the carbon isotopic composition of seawater. This study presents bulk isotopic and elemental analyses from fine-grained siliciclastics of the Late Devonian–Early Mississippian Bakken Formation (Williston Basin, USA) to assess the volume and isotopic composition of carbonates in these sediments. Carbonate in the Bakken black shales occurs primarily as microscopic disseminated dolomite rhombs and calcite cements that, together, comprise a significant mass-fraction (*ca* 9%). The elemental composition of the shales is indicative of a dynamic anoxic to sulphidic palaeoenvironment, likely supported by a fluctuating chemocline. Despite forming in an environment favourable to remineralization of organic matter and the precipitation of isotopically depleted authigenic carbonates, the majority of carbon isotope measurements of disseminated carbonate fall between $-3‰$ and $+3‰$, with systematically more depleted carbonates in the deeper-water portions of the basin. Thus, although there is evidence for a significant total mass-fraction of carbonate with contribution from remineralized organic matter, Bakken authigenic carbonates suggest that Famennian black shales are unlikely to be sufficiently ^{13}C -depleted relative to water column dissolved inorganic carbon to serve as a major lever on seawater isotopic composition.

Keywords Authigenic carbonate, Bakken Formation, black shale, Devonian, Hangenberg Event.

INTRODUCTION

Over geological timescales, the carbon input to the ocean-atmosphere system from outgassing of the solid Earth is balanced by two main sinks: burial of both marine carbonate minerals and sedimentary organic carbon (Holland, 1978; Garrels & Lerman, 1981; Berner, 2003). Because the formation of reduced organic carbon through oxygenic photosynthesis ensures a net release of O_2 and drawdown of CO_2 when buried for long time intervals, the climate and redox state of the Earth's surface is inherently tied to the global carbon cycle (Broecker, 1970; Garrels & Lerman, 1981). This link makes carbon cycle models and proxies an important resource for reconstructing ancient environments. The proportional burial of carbon in each form (marine carbonate, f_{MC} and organic carbon, f_{OC}) can be estimated from the stable carbon isotopic composition of marine dissolved inorganic carbon ($\delta^{13}C_{DIC}$), where the majority of surface inorganic carbon resides. Photosynthesis entails a kinetic isotope effect ($\epsilon_p \approx 25\text{‰}$, written positive by convention) which leaves organic carbon isotopically depleted with respect to ^{13}C , so increased f_{OC} will drive $\delta^{13}C_{DIC}$ to more enriched values. Conversely, the precipitation of primary marine carbonates from DIC entails only a minor fractionation (Emrich *et al.*, 1970), so the carbon isotopic composition of limestones is commonly employed as a proxy for long-term trends in f_{MC} and f_{OC} . The $\delta^{13}C$ record can therefore inform models for the oxygenation of the ocean-atmosphere system (e.g. Broecker, 1970; Garrels & Lerman, 1981; Kump & Garrels, 1986; Des Marais *et al.*, 1992; Karhu & Holland, 1996; Kump *et al.*, 2011) and evolution of Earth's climate (e.g. Arthur *et al.*, 1985; Berner, 1991; Kump & Arthur, 1999).

Significant deviations in the covariation between $\delta^{13}C_{DIC}$ and atmospheric pO_2 proxies, particularly with regard to large carbon-isotope excursions (CIEs) and anomalously high $\delta^{13}C_{DIC}$ baselines in the Proterozoic, have led to the development of alternatives to the two-sink carbon model (Dickens, 2003; Hayes & Waldbauer, 2006; Schrag *et al.*, 2013; Shields & Mills, 2017). The model proposed by Schrag *et al.* (2013) attempts to reconcile conflicting trends in $\delta^{13}C$ and Earth's redox budget by invoking authigenic carbonates as a third major sink for carbon. Authigenic carbonates are formed diagenetically within sedimentary pore spaces, often precipitating when the anaerobic oxidation of organic

carbon or methane induces carbonate supersaturation with an isotopically depleted $\delta^{13}C$ composition (Berner, 1968; Raiswell, 1976; Curtis & Coleman, 1986; Coleman & Raiswell, 1993). In the modern ocean, the formation of low- $\delta^{13}C$ authigenic cements is typically limited to reducing environments rich in organic matter which promote sulphate-reducing microbial metabolisms, such as tropical river deltas (Zhu *et al.*, 2002) and sea floor methane seeps (e.g. Peckmann *et al.*, 2001; Formolo *et al.*, 2004). The global burial of authigenic carbonate is therefore suppressed in the well-oxygenated modern ocean (Mitnick *et al.*, 2018; Bradbury & Turchyn, 2019). However, Higgins *et al.* (2009) hypothesize that Proterozoic ocean conditions with a diminished biological pump, a larger DIC reservoir and low pO_2 levels promoted an elevated sea floor carbonate saturation state and anaerobic respiration of organic carbon. The widespread occurrence of sea floor carbonate fans and other anomalous cements in the Proterozoic supports this assertion (e.g. Grotzinger & Knoll, 1995; Grotzinger & James, 2000; Pruss *et al.*, 2008; Bergmann *et al.*, 2013). In this manner, ancient oceans may have possessed a third carbon sink with a depleted $\delta^{13}C$ inherited from remineralized organic carbon. Significant rates of authigenic carbonate burial could force $\delta^{13}C_{DIC}$ to more enriched values, driving a positive CIE without oxygenating the atmosphere as organic carbon burial would. The authigenic model therefore represents a means to decouple the $\delta^{13}C$ time series and pO_2 trends, which would require a significant re-evaluation of carbon cycle interpretations and modelling approaches.

A corollary hypothesis to the above model is that episodes of global marine anoxia in the Phanerozoic may have forced a return to Proterozoic oceanic conditions and augmented authigenic carbonate burial rates. Increased anaerobic respiration of organic matter during anoxia could induce porewater supersaturation with respect to $CaCO_3$, while the collapse of the biological pump resulting from a mass extinction could drive the sea floor carbonate saturation state upward (Higgins *et al.*, 2009). Conspicuous authigenic carbonate deposits may therefore be preserved during critical Phanerozoic environmental perturbations, such as the end-Permian mass extinction or the Late Devonian anoxic events (Higgins *et al.*, 2009; Schrag *et al.*, 2013). Indeed, Lower Triassic carbonate precipitates have previously been compared to

Proterozoic-style fans formed during supersaturated conditions (Grotzinger & Knoll, 1995; Pruss *et al.*, 2006; Baud *et al.*, 2007; Woods & Baud, 2008; Bergmann *et al.*, 2013). However, despite similar environmental stressors including widespread ocean anoxia, increased organic carbon burial and a mass extinction of metazoan calcifiers (Copper, 1994; Grotzinger & Knoll, 1995), the Late Devonian has received less attention than other Phanerozoic time periods in the search for anomalous carbonate sedimentation.

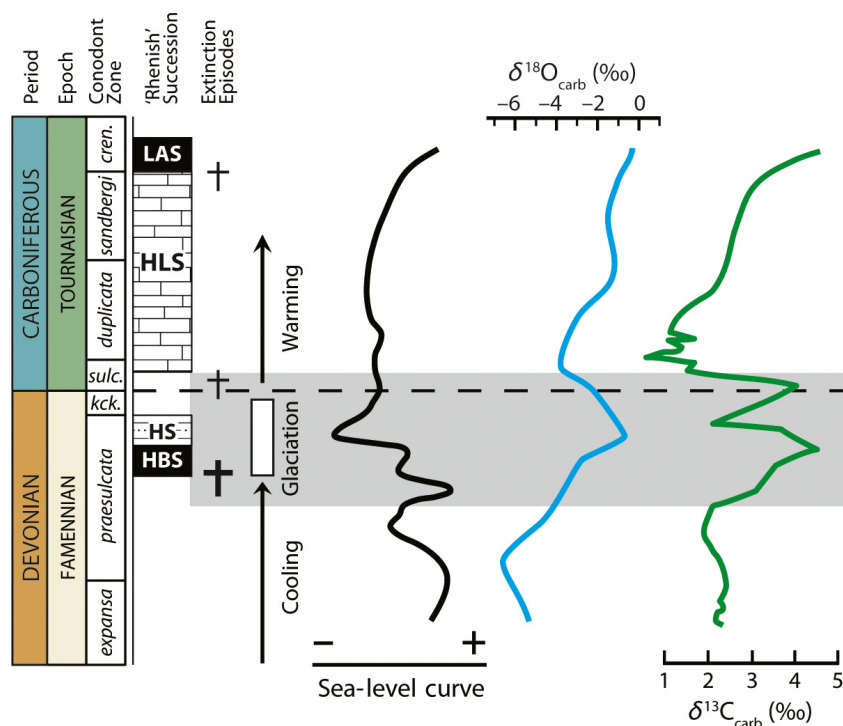
The present study utilizes carbonate-carbon isotopic and bulk rock elemental and mineralogical data to assess the mass and isotopic composition of authigenic carbonate in the Late Devonian–Early Mississippian Bakken Formation. The Bakken comprises two organic-rich shale members which reflect pervasive reducing conditions and therefore a likely host for disseminated isotopically depleted authigenic carbonates. The economic importance of the Bakken as a closed-fluid source system (Price & LeFever, 1992; Gaswirth *et al.*, 2013) has motivated a long history of drill core sampling and geochemical analyses, allowing new results to build upon a large body of existing data. This work therefore serves as a case study for bulk geochemical approaches to estimating authigenic carbonate mass and composition to test the authigenic model at a large scale.

GEOLOGICAL CONTEXT

End-Devonian Hangenberg Event

The Late Devonian epoch was characterized by a series of biotic crises which together comprise one of the ‘Big Five’ mass extinction events (Raup & Sepkoski, 1982). The Hangenberg (*ca* 358.9 Ma), occurring just before the Devonian–Carboniferous Boundary, is the final event in a protracted series of Devonian extinctions. The Hangenberg extinction was accompanied by widespread ocean anoxia and a positive carbon-isotope excursion of *ca* 4‰, followed by a sea-level regression and glaciation (Fig. 1; Caplan & Bustin, 1999; Brand *et al.*, 2004; Buggisch & Joachimski, 2006; Kaiser *et al.*, 2006; Cramer *et al.*, 2008; Isaacson *et al.*, 2008; Kumpan *et al.*, 2015; Qie *et al.*, 2015; Becker *et al.*, 2016; Kaiser *et al.*, 2016). This interval is marked globally by a lithostratigraphic succession of the transgressive ‘Hangenberg Black Shale’ overlain by upward-coarsening siliciclastics deposited during the Hangenberg regression (Kaiser *et al.*, 2016). The global deposition and preservation of the organic-rich black shales has been variably attributed to upwelling nutrient-rich anoxic bottom waters during the transgression (Caplan & Bustin, 1998, 1999; Marynowski *et al.*, 2012; Formolo *et al.*, 2014) or a shallow-water nutrient flux triggering a

Fig. 1. Biostratigraphy, lithostratigraphy and chemostratigraphy across the Devonian–Carboniferous Boundary. Conodont zonation modified from Kaiser *et al.* (2009); *kck.*, *kockeli*; *sulc.*, *sulcata*; *cren.*, *crenulata*. Lithostratigraphy modified from the ‘Rhenish Standard Succession’ of Becker *et al.* (2016); HBS, Hangenberg Black Shale; HS, Hangenberg siltstone/sandstone; HLS, Hangenberg limestone; LAS, Lower Alum Shale. Sea-level trends after Bless *et al.* (1993), climate and general $\delta^{18}\text{O}_{\text{carb}}$ after Mii *et al.* (1999) and Brand *et al.* (2004), and general $\delta^{13}\text{C}_{\text{carb}}$ after Mii *et al.* (1999) and Buggisch & Joachimski (2006).



eutrophication event (Carmichael *et al.*, 2016, and references therein). Regardless of the triggering mechanism, during this interval anoxic and possibly euxinic conditions extended up into shallow marine environments and contributed to the mass extinction.

One important consequence of the Hangenberg Event was the ‘global carbonate crisis’, a sudden reduction in carbonate lithologies immediately above the Hangenberg Black Shale (Kaiser *et al.*, 2016). This transition to predominantly siliciclastic lithologies is well-represented in Laurentia by a series of Famennian black shales unconformably overlying carbonate units (Figs 2 and 3). The Hangenberg mass extinction had the greatest ecological impact on reef-building metazoans, causing the extinction of stromatoporoid sponges and severely reducing rugose and tabulate coral diversity (Copper, 1994; McGhee *et al.*, 2013). The extinction of the dominant reef-builders, in tandem with the major base-level fluctuations (Fig. 1; Kaiser *et al.*, 2016) were likely linked to

the global carbonate crisis. As a result, Hangenberg limestones are very condensed and no known reef complex survived into the Carboniferous (Kaiser *et al.*, 2016). The end-Devonian reduction of metazoan calcifiers coincides with observed peaks in calcimicrobial mud mounds (Kiessling, 2002; Webb, 2002), cyanobacterial calcification (Arp *et al.*, 2001; Riding, 2006, 2009), ooid abundance (Sandberg, 1983; Wilkinson & Given, 1986) and reefal cements and micrite (Kiessling, 2002; Webb, 2002). In aggregate, these trends are hypothesized to represent a relative high in calcite saturation state (Webb, 1996; Riding & Liang, 2005; Riding, 2006; Yao *et al.*, 2016). Given the above evidence, the Devonian–Carboniferous boundary – marked by high organic carbon burial, global marine anoxia, a genetic shift in carbonate deposition and high carbonate saturation state – embodies a Phanerozoic interval in which elevated burial of isotopically depleted authigenic carbonate could contribute to a positive carbon-isotope excursion.

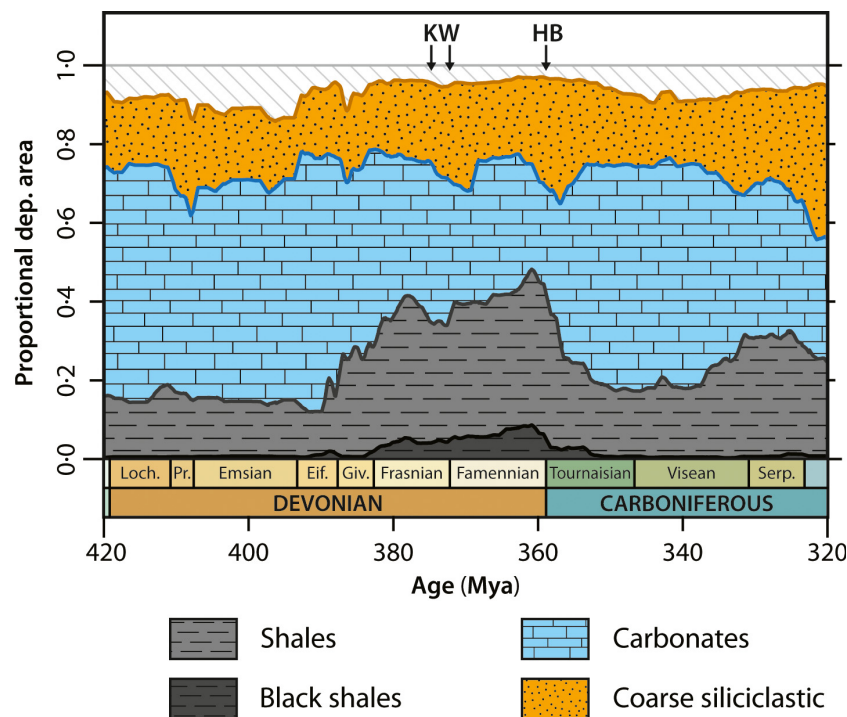


Fig. 2. Depo-preservational trends in North American sedimentary lithologies through the Devonian and Carboniferous from the Macrostrat database. Proportional deposition–preservation was calculated from lithological classifiers associated with units within 949 North American geospatial polygons: $\sum[(\text{area of polygon} * \text{proportion of lithotype}) / (\text{total N.A. depositional area})]$. The time series was estimated for 10^5 -year time bins. Macrostrat database methods after Peters *et al.* (2018). ‘Black shales’ represent shale units with the lithological classifier ‘black’; ‘coarse siliciclastics’ comprise siltstones, sandstones, conglomerates and breccia. Unfilled area at top (hatched fill) corresponds to unclassified, evaporite or organic lithologies. KW, Kellwasser events; HB, Hangenberg Event; Loch., Lochkovian; Pr., Pragian; Eif., Eifelian; Giv., Givetian; Serp., Serpukhovian.

Bakken Formation

The Bakken Formation is a subsurface unit whose extent is known from drill cores in southern Manitoba and Saskatchewan, north-eastern Montana and north-western North Dakota (Figs 3 and 4A). It is recognized in cores by its distinctive stratigraphic succession of three informal members (Figs 4B and 5): the Lower Bakken black shale (LBS), the Middle Bakken dolomitic siltstone to sandstone (MB) and the Upper Bakken black shale (UBS). Deposition took place through the Late Devonian–Early Carboniferous in the Williston Basin, a shallow intracratonic setting at the southernmost end of the Western Canada Sedimentary Basin. The Bakken was deposited coeval with a suite of black shale lithologies in epeiric basins across Laurentia (Algeo *et al.*, 2007), including the neighbouring Exshaw and basal Banff shales of Western Canada and the Sappington Formation of Montana (Fig. 3; Smith *et al.*, 1995; Smith & Bustin, 2000). The formation has been traditionally interpreted as one parasequence bounded by two transgressive black shales (Webster, 1984; Smith *et al.*, 1995; Smith & Bustin, 1996, 2000; *cf.* interpretations by Egenhoff, 2017). Estimates of the Bakken Formation's age rely on a sparse biostratigraphic record: on the basis of conodont assemblages, the onset of Lower Bakken sedimentation has been constrained to the Late Famennian, and the top of the Upper Bakken to the Middle Tournaisian (Johnston *et al.*, 2010). The

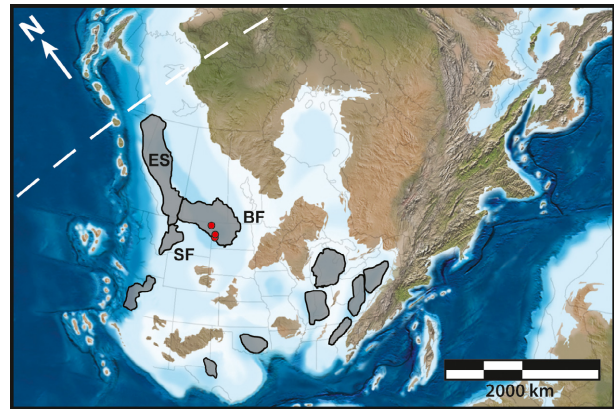


Fig. 3. Palaeogeographic distribution of Laurentian 'black-shale seas' at 360 Ma. Palaeo-reconstruction of the Late Devonian modified from Blakey (2016). Studied core locations marked by red dots, and the palaeo-latitude of the equator by the dashed white line. BF, Bakken Formation; ES, Exshaw Shale; SF, Sappington Formation.

distinctive shale–sandstone succession has been hypothesized to correspond to the Hangenberg Black Shale holotype from Europe (Becker *et al.*, 2016; Kaiser *et al.*, 2016), but efforts to assign the stratigraphic position of the Hangenberg Event based on fossil assemblages (Thrasher, 1987), miospore and acritarch biostratigraphy (Playford & McGregor, 1993), or sequence stratigraphy (Egenhoff, 2017) have yet to reach a consensus.

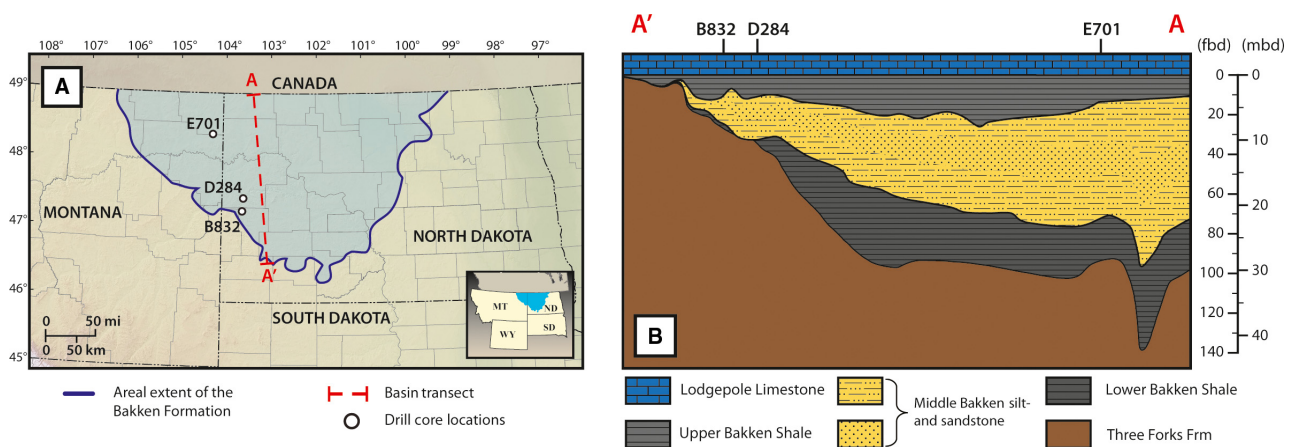


Fig. 4. Areal extent and stratigraphy of the Bakken Formation, Williston Basin. (A) Map of the modern extent of the Bakken Formation in the United States, modified from Gaswirth *et al.* (2013). Study core locations marked and labelled. (B) Stratigraphic cross-section of the Williston Basin. Basin transect as marked in (A), with approximate relative locations of study cores labelled. Unit thickness data from isopachous maps in Lefever (2008), using the top of the Upper Bakken Shale as the datum horizon. fbd, feet below datum; mbd, metres below datum.

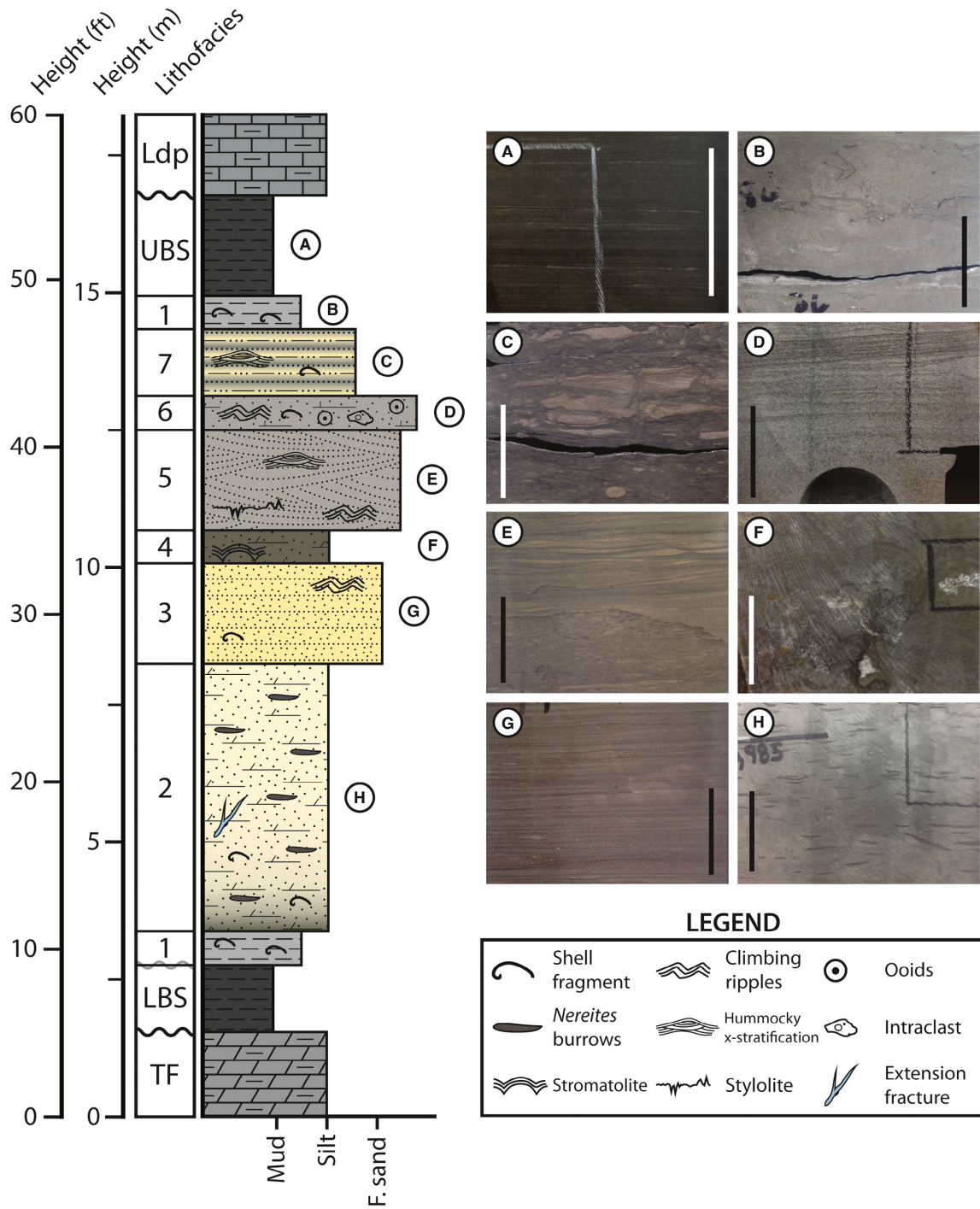


Fig. 5. Generalized stratigraphy of the Bakken Formation in the studied cores. Middle Bakken lithofacies classifications modified from Egenhoff *et al.* (2011); LBS, Lower Bakken black shale; Ldp, Lodgepole Limestone; TF, Three Forks Formation; UBS, Upper Bakken black shale. Note the disconformities bounding the Bakken Formation (bold wavy lines) and the semi-conformable surface above the Lower Bakken shale (faded wavy line). (A) Organic-rich black shale with visible fine silt laminae. (B) Skeletal wackestone (facies 1). (C) Alternating siltstone/mudstone beds disrupted by hummocky cross-stratification and bioturbation (facies 7). (D) Fine-grained oolitic and intraclastic quartz sandstone (facies 6). (E) Cross-bedded fine sandstone (facies 5). (F) Laminated microbial bindstone with cement-filled fenestrae (facies 4). (G) Horizontally laminated siltstone to fine sandstone with occasional climbing ripples (facies 3). (H) Calcareous siltstone with pervasive mud-infilled *Nereites* burrows and occasional skeletal fossils (facies 2). White and black bars measure 1" (2.5 cm) in all photographs.

Most palaeoenvironmental interpretations propose that the Bakken black shales were deposited in a stratified, restricted basin where bottom-water anoxia was maintained by increased primary productivity and a coincident marine transgression (Lineback & Davidson, 1982; Smith & Bustin, 1998). An alternative model for the black shales' organic preservation is water-column euxinia – oxygen-depleted and sulphide-rich conditions – throughout the Williston Basin (Scott *et al.*, 2017). Long-term anoxia in the bottom waters may have promoted sulphate-reducing microbial (SRM) communities which drove sulphide concentrations higher, forcing euxinic waters up into the photic zone. The shoaling of the chemocline has been previously proposed as a Late Devonian extinction mechanism (Kump *et al.*, 2005; Marynowski & Filipiak, 2007) and hypothesized in neighbouring epeiric basins (Formolo *et al.*, 2014). Euxinic conditions account for the Bakken enrichment of trace metals which are sensitive to anoxic-sulphidic sedimentation (Algeo & Tribouillard, 2009; Scott *et al.*, 2017), as well as abundant aryl isoprenoids (Requejo *et al.*, 1992; Jiang *et al.*, 2001; Aderoju & Bend, 2018). These biomarkers are a proxy for *Chlorobiaceae*, obligate phototrophic green sulphur bacteria which live in photic-zone sulphidic environments (Summons & Powell, 1986).

MATERIALS AND METHODS

Preliminary geochemical data from the Bakken Formation were compiled from the USGS Core Research Center Well Catalog (USGS CRC, 2016). Over 2000 measurements comprising LECO and Rock-Eval, X-ray diffraction (XRD) and X-ray fluorescence (XRF) analyses were obtained across 25 cores from Montana and North Dakota. Three USGS slabbed drill cores were selected for sampling: library numbers B832 (BN 1-23H: 47°11'40"N, 103°34'06"W); D284 (15-22 BN Flat Top Butte: 47°27'57"N, 103°32'12"W); and E701 (1 Big Sky HD: 48°22'46"N, 104°08'09"W). The cores form a *ca* 138 km transect within the Williston Basin, from basin-central in the north to basin-marginal in the south (Fig. 4). A total of 100 rock cut and powder samples were collected throughout the Bakken members and underlying Three Forks Formation. Sampling targeted lithofacies boundaries at the finest resolution, with mean

sampling intervals of *ca* 6 inches (*ca* 15.25 cm) through black shale members and *ca* 2 feet (*ca* 61 cm) through more homogeneous Middle Bakken facies (imperial units are used by CRC convention). All rock powders were collected within a <1" (2.5 cm) vertical window using a Dremel rotary drill outfitted with a tungsten carbide cutter bit. Prior to sampling, the external layer of the core was abraded and discarded to avoid contamination. Seventeen rock cuts were later vacuum-impregnated in epoxy, ground to 30 μm , and prepared as covered thin sections.

Following sampling, stable carbon and oxygen isotopic analyses were performed on a total of 123 rock powders by the University of Michigan Stable Isotope Laboratory. The samples were reacted with anhydrous phosphoric acid heated to 77°C in a Finnigan MAT Kiel IV device and the resulting CO₂ gases analyzed by a Finnigan MAT 253 triple-collector isotope ratio mass spectrometer (IRMS; Thermo Fisher Scientific, Waltham, MA, USA). All carbon and oxygen isotope ratios were reported in per mil (‰) relative to the V-PDB (Vienna Pee Dee Belemnite) standard. Session calibration measurements were performed with NBS 19 calcite standards, yielding an internal standard deviation precision (1σ) of 0.051‰ for $\delta^{13}\text{C}$ and 0.054‰ for $\delta^{18}\text{O}$ ($n = 32$). Three replicate samples yielded a 1σ precision of 0.17‰ for $\delta^{13}\text{C}$ and 0.098‰ for $\delta^{18}\text{O}$. Selected outlier samples were re-run at the University of Washington IsoLab to test replicability and potential sample heterogeneity. Powders there were reacted with phosphoric acid in a Kiel III carbonate device before transfer to a dual-inlet Finnigan Delta Plus IRMS (Thermo Fisher Scientific). Internal reference materials established a 1σ precision of 0.068‰ for $\delta^{13}\text{C}$ and 0.070‰ for $\delta^{18}\text{O}$ ($n = 11$), while five UWC-3 carbonate standards (Kozdon *et al.*, 2009) yielded a precision of 0.015‰ for $\delta^{13}\text{C}$ and 0.096‰ for $\delta^{18}\text{O}$. The mean reproducibility between the results of the two laboratories across 19 replicate samples was 0.12‰ for $\delta^{13}\text{C}$ and 0.15‰ for $\delta^{18}\text{O}$, which is smaller than the magnitude of the chemostratigraphic variability observed in either core.

Elemental abundances were measured in each rock powder sample using a Thermo Fischer Scientific Niton XL3t GOLDD + handheld XRF analyzer mounted at the Wisconsin Geological & Natural History Survey following measurement and reference standard methods described in Zambito *et al.* (2016). Powders were mixed and

each vial inverted against a polypropylene film over the XRF analyzer window. Five pressed standards were measured throughout the session to calibrate raw data: USGS reference standards SBC-1, SDO-1 and COQ-1; NIST standard SRM-1d; and Thermo Scientific Blank 180-647. Absolute precision (1σ) for the reference standards averaged <5% for major elements Ca, Sr, Si, Al, Fe and S. Results included calculated atomic ppm and error estimates for a suite of 43 elements, as well as the total balance measurement to screen for matrix effects.

RESULTS

Sedimentology

Detailed stratigraphic observations and samples were made for cores D284 and E701, which represent basin-marginal and basin-central positions, respectively (Fig. 5). In hand samples, the Upper and Lower black shale members are lithologically similar (Fig. 5A): clay-rich and organic-rich mudstones interrupted by detrital silt laminae (interpreted as high-energy storm inputs to the deeper parts of the basin), pyrite microveins and framboids, and scattered conodonts. Macroscopic carbonate content in the shale is limited to rare skeletal fossils. In contrast, the Middle Bakken member incorporates a diversity of carbonate-rich lithofacies deposited in more oxic conditions (classification scheme after Egenhoff *et al.*, 2011). The lowermost facies coarsen upward from a carbonaceous siltstone replete with mud-filled *Nereites* burrows (Fig. 5H) to interbedded planar siltstone–fine sandstone (Fig. 5G), and in core D284 a lagoonal microbial bindstone facies with calcite cement-filled fenestrae (Fig. 5F). Shallower carbonaceous fine to medium sandstones facies occur above this boundary, with bedding ranging from massive to hummocky cross-stratified (Fig. 5E) and occasional beds of coarser cross-bedded quartz sandstone featuring irregular ooids and intraclasts (Fig. 5D). The coarsening trend in the lower two-thirds of the Middle Bakken member is overlain by upward fining units, including a finer intercalated sandstone and siltstone facies (Fig. 5C) through the uppermost third of the Middle Bakken to the base of the Upper Bakken black shale. Carbonate wackestones with infrequent rhynchonella brachiopods typically occur at the top and base of the Middle Bakken (Fig. 5B).

In petrographic thin section, black shale samples exhibit diverse microtextures (Fig. 6). Silt laminae (Fig. 6A) are predominantly composed of detrital quartz grains, with less abundant mixtures of detrital and diagenetic dolomite and possible calcite cement. In the fine mud matrix, compressed radiolarians and *Tasmanites* algal cysts occur in discrete beds and have commonly undergone diagenetic replacement by silica and pyrite (Fig. 6B). Infrequent primary skeletal grains (*ca* 1000 μm) are often masked by diagenesis, whereas abundant subhedral to euhedral dolomite grains (<10 μm) are disseminated throughout the mud matrix (Fig. 6C). Dolomite rhombs that lack clear axis orientations suggest an authigenic origin (Saitoh *et al.*, 2015), whereas subhedral and weathered dolomite grains with general bedding orientation likely reflect a detrital origin (Fishman *et al.*, 2015). Authigenic silica, dolomite and framboidal pyrite are frequently concentrated around organic carbon-rich zones and silt laminae (Fig. 6D). Middle Bakken thin sections feature abundant carbonate cements (Fig. 6E) and pervasive dolomitization of primary fabrics (Fig. 6F). Siltstones are primarily composed of clays, detrital quartz and micrite mud. Macrofossil fragments, where present, are altered by authigenic dolomite and speckled with fine authigenic pyrite grains. Sandstone facies feature fine to medium quartz grains which accommodate interstitial carbonate and minor anhydrite cements, whereas coarser sandstones include infrequent reworked ooids, intraclasts and biogenic grains (Fig. 6F).

Compiled geochemical data (USGS CRC, 2016) show that the Bakken black shales are predominantly quartz and clay (Fig. 7; Table 1). The Upper Bakken is distinguished by higher proportions of quartz, carbonate and total organic carbon (TOC), whereas the Lower Bakken is comparatively richer in clays and potassium feldspar. Each member contains heterogeneous enrichments of carbonate (*ca* 9 wt.%) and pyrite (*ca* 6.5 wt.%; Fig. 7). Dolomite constitutes the majority of the Upper and Lower black shale carbonates (*ca* 85% of all carbonates). By contrast, the Middle Bakken averages *ca* 47.6 wt.% carbonate mineralogy, of which *ca* 31% is calcite. Quartz and clays comprise the siliciclastic component, which decrease up-section as carbonate mass increases in the shallower facies towards the top of the member. Also of note is the presence of significant pyrite and anhydrite in some cores, ranging up to 17% and 40%, respectively.

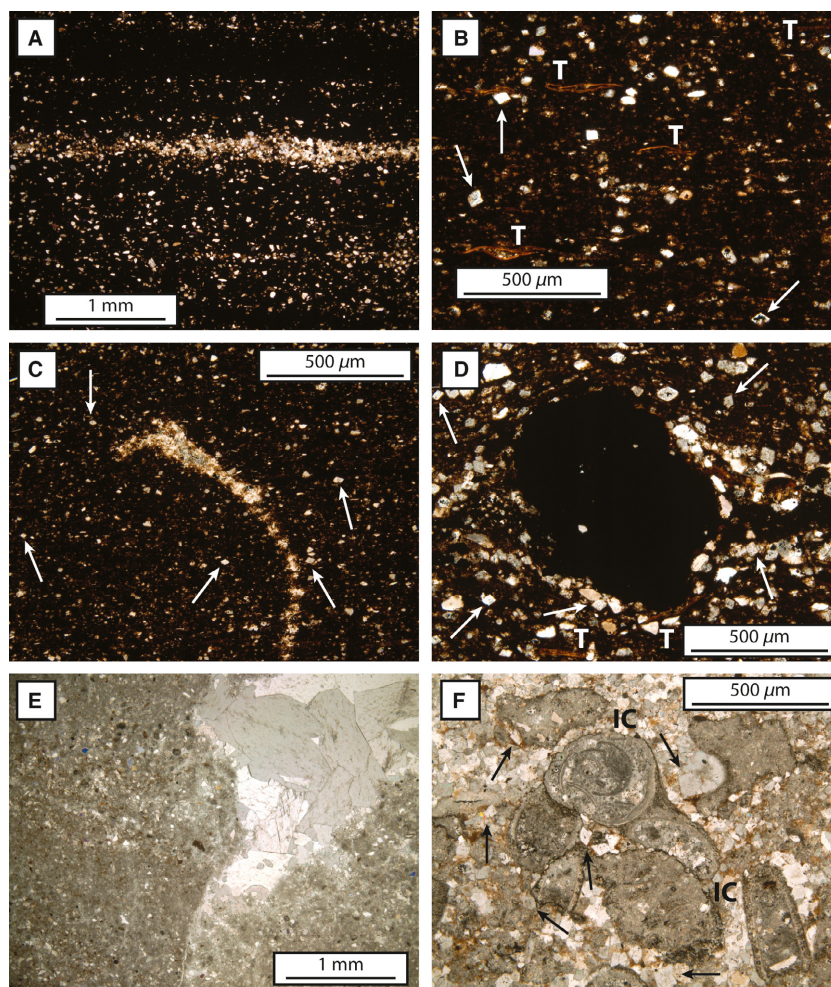


Fig. 6. Cross-polarized photomicrographs of Bakken primary and secondary carbonate features. (A) Discrete $\leq 200 \mu\text{m}$ -scale horizontal quartz-rich and dolomite-rich silt laminae in the Upper Bakken (D284, 10 965'; 3342.1 m). (B) Closer detail of the mud matrix, disseminated *ca* $25 \mu\text{m}$ euhedral dolomite rhombs with no consistent axial orientation (arrows) and collapsed *Tasmanites* algal cysts (T) which commonly serve as the loci for silica and pyrite diagenesis. Sample from the Lower Bakken (E701, 9925.3'; 3025.2 m). (C) A brachiopod shell fragment altered by diagenesis. Disseminated euhedral dolomite rhombs speckle the mud matrix (arrows); from the Upper Bakken (B832, 10 356.4'; 3156.6 m). (D) Silt laminae bedded around a large ($>500 \mu\text{m}$) pyrite framboid. Note the associated occurrence of dolomite rhombs (arrows) and *Tasmanites* algal cysts (T); from the Lower Bakken (E701, 9925.3'; 3025.2 m). (E) Fenestral pore within the Middle Bakken microbial bindstone facies, infilled by coarsely crystalline carbonate cement. Note the stromatolitic laminae in the micrite-silt matrix, distinguished by alternating fine and coarse grains (D284, 10 969.35'; 3343.5 m). (F) Fine-medium silty-sandstone facies featuring intraclastic grains (IC) with edge deterioration suggestive of reworking and dissolution. Within these Middle Bakken facies, dolomitization has visibly impacted much of the carbonate matrix (arrows; D284, 10 967'; 3342.7 m).

Stable isotopic compositions

The two main study cores feature a wide range of $\delta^{13}\text{C}_{\text{carb}}$ values (Figs 8 and 9; Table 2), from -2.4 to $+3.9\text{‰}$ _{VPDB} in basin-marginal core D284 (mean = $+0.7\text{‰}$) and from -6.8 to $+0.3\text{‰}$ in basin-central core E701 (mean = -1.3‰). Average isotopic values throughout E701 are more depleted than D284 by *ca* 2.0‰ , and within each

core the black shale members tend towards more depleted $\delta^{13}\text{C}$ compositions (mean = -1.1‰) relative to the oxic Middle Bakken (mean = -0.25‰). The $\delta^{18}\text{O}_{\text{carb}}$ measurements show more moderate variation. When $\delta^{13}\text{C}$ and $\delta^{18}\text{O}$ are plotted against the compositional range of Late Devonian and Early Mississippian brachiopods (Fig. 9), the oxygen data fall largely within the range of observed values, whereas almost all

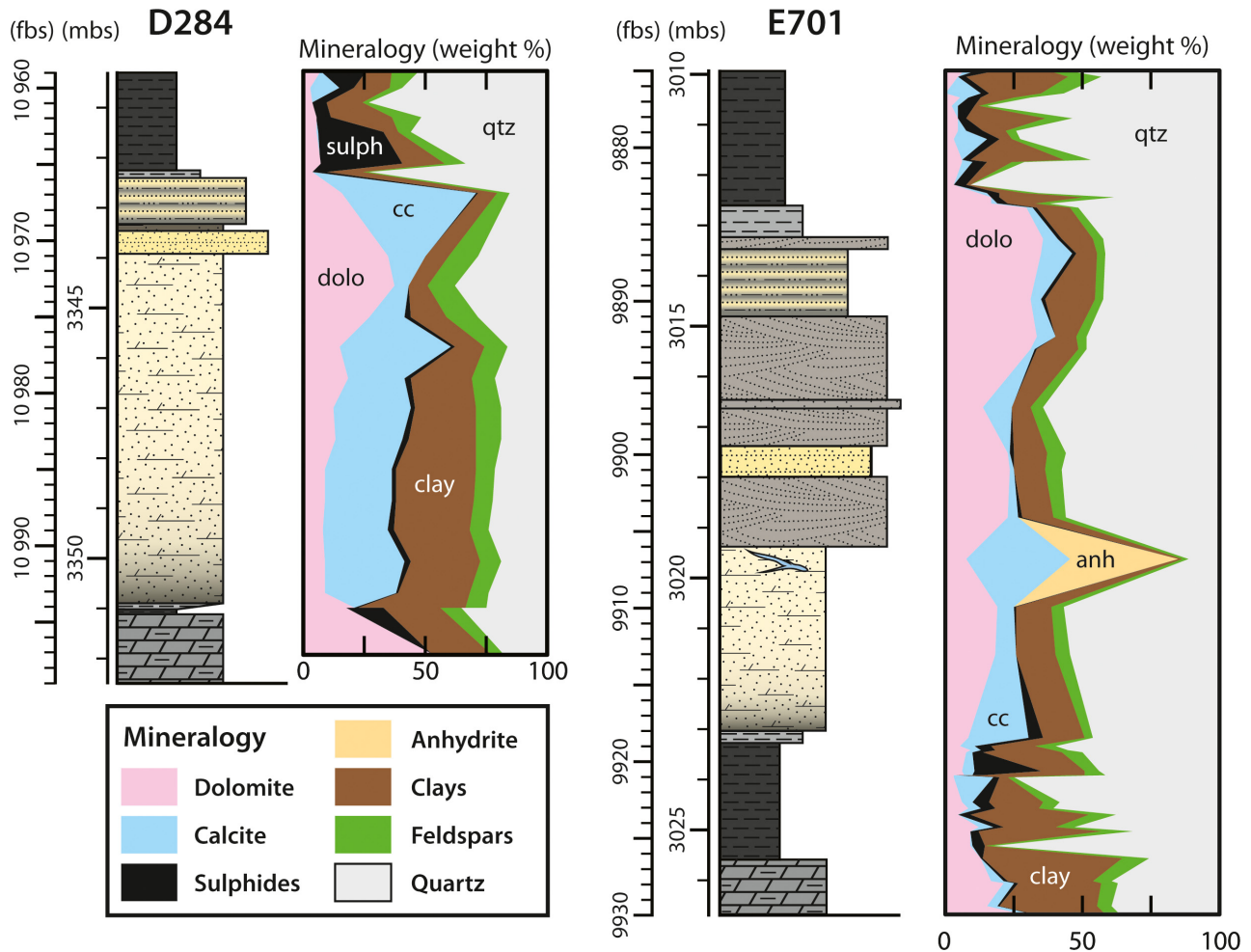


Fig. 7. Bulk mineral chemostratigraphy through the Bakken Formation. X-ray diffraction (XRD) measurements (cumulative weight %) from the studied Bakken cores compiled from the USGS Core Research Center database. All lithofacies' colours and textures correspond the general stratigraphic column in Fig. 5. Note the mineral data for E701 at 9906-9' (3019.6 m) represents a sampled late-diagenetic vein infilled with calcite and anhydrite. 'Feldspars' comprise both plagioclase and albite minerals. cc, calcite; fbs, feet below surface; mbs, metres below surface.

carbon data are depleted relative to the aggregate range. The reported $\delta^{13}\text{C}$ values are comparable to previous $\delta^{13}\text{C}$ measurements of Middle Bakken carbonates, which fall between -6.3‰ to $+4.6\text{‰}$ (Pitman *et al.*, 2001; Brennan, 2016; Brodie *et al.*, 2018). These bulk measurements represent admixtures of the Bakken primary and diagenetic carbonate phases; analyses from the secondary ion mass spectrometer (SIMS) resolve *in situ* variability in Middle Bakken cement phases' $\delta^{13}\text{C}$ from *ca* -15‰ to $+5\text{‰}$ (Denny *et al.*, 2019).

Within each core, there is only a weak and inconsistent correlation between $\delta^{13}\text{C}_{\text{carb}}$ and $\delta^{18}\text{O}_{\text{carb}}$ (E701: Spearman's $\rho = 0.0288$; D284:

$\rho = -0.165$). However, $\delta^{13}\text{C}$ and $\delta^{18}\text{O}$ covariation is more consistent when individual lithologies are considered: isotopic data from the carbonate wackestone shows a strong positive correlation ($\rho = 0.810$, $n = 8$), as does Upper Bakken black shale data from E701 ($\rho = 0.579$, $n = 16$) and all black shale data from D284 ($\rho = 0.837$, $n = 18$). Strong covariations in carbonate stable carbon and oxygen isotopic data are commonly interpreted as indicators of meteoric-seawater mixing diagenesis, when the pore fluid geochemistry evolves with increasing carbonate sourced from organic matter and $\delta^{18}\text{O}$ -fractionated meteoric water (Allan & Matthews, 1982; Lohmann, 1988). This process should be most pronounced

Table 1. Bulk organic carbon (LECO–TOC) and mineralogical (XRD) mean and range statistics for the Bakken Formation members. LBS, Lower Bakken black shale; MB, Middle Bakken siltstone to sandstone; UBS, Upper Bakken black shale. Compiled from the USGS Core Research Center database. For TOC data, $n_{\text{UBS}} = 312$, $n_{\text{MB}} = 371$ and $n_{\text{LBS}} = 311$; for XRD data, $n_{\text{UBS}} = 166$, $n_{\text{MB}} = 73$ and $n_{\text{LBS}} = 68$. TOC, total organic carbon.

	wt. %	TOC	Quartz	K Feldspar	Plagioclase	Calcite	Dolomite	Pyrite	Sphalerite	Anhydrite	Clays
UBS	Mean	10.60	50.4	7.93	1.66	1.44	8.83	6.52	0.58	0.029	21.8
	Range	(0.76 to 25.3)	(14.4 to 90.7)	(0 to 23)	(0 to 7)	(0 to 21)	(0 to 34)	(0 to 34)	(0 to 16)	(0 to 2)	(1.42 to 60.3)
MB	Mean	0.49	28.3	5.05	0.00	14.80	32.80	1.16	0.032	1.06	14.8
	Range	(0 to 10.4)	(4 to 64.2)	(0 to 13)	–	(0 to 84)	(2 to 77)	(0 to 17)	(0 to 2.3)	(0 to 39.6)	(0 to 58)
LBS	Mean	9.19	44.6	9.81	0.83	1.12	5.64	6.71	0.19	0.00	29.9
	Range	(0.45 to 23.8)	(19 to 82.4)	(2 to 25)	(0 to 5)	(0 to 16)	(1 to 21)	(1 to 24)	(0 to 5.2)	–	(0.1 to 60.7)

in shallow, porous and permeable lithologies susceptible to groundwater influx from a landscape that features a terrestrial biosphere. The above interpretations cannot be treated as diagnostic, however, as additional alteration mechanisms may induce $\delta^{13}\text{C}$ to $\delta^{18}\text{O}$ covariation, or conversely, heavily altered bulk carbonate may exhibit no such correlation (Swart & Oehlert, 2018). In the Bakken system, the diverse lithologies seem to exert a primary control on the carbonate isotopic composition. Regardless, the burial of depleted- $\delta^{13}\text{C}$ carbonates formed through either meteoric mixing or carbonate authigenesis, *sensu* Schrag *et al.* (2013), will both drive similar trends in $\delta^{13}\text{C}_{\text{DIC}}$ on a potentially global scale (e.g. Dyer *et al.*, 2015).

Elemental geochemistry

Hand-held X-ray fluorescence elemental abundance data from bulk rock samples represent useful proxies for evaluating the depositional palaeoenvironment. Elemental redox proxies reflect reducing settings in which certain elements settle out of solution (Mo, U and V) or react with H_2S to form metal sulphides (Cu, Ni, Pb and Zn; Tribouillard *et al.*, 2006; Calvert & Pedersen, 2007). Manganese accumulates in anoxic or alternating oxic–anoxic settings. Reduced Mn is soluble and can be incorporated into carbonates or sulphides, whereas oxidizing conditions produce Mn-oxides (Lepland & Stevens, 1998). Additional elemental proxies include indicators of detrital sedimentation (Si, Al, K, Cr, Rb, Ti and Zr) and carbonate sedimentation (Ca, Mg and Sr). The elemental data are presented normalized to the conservative element Al, which reduces error from absolute measurement variation (Calvert & Pedersen, 2007), and are compared to an ‘average’ shale composition from Wedepohl (1971) for reference (Tables 3 and S1). In the black shales each of the redox proxies is significantly enriched and Mn/Al is depleted; of particular note are the Mo and Zn data, which exhibit ‘hyper-enrichments’ two to three orders of magnitude higher than the reference shale (Scott *et al.*, 2017). These proxies’ stratigraphic trends through the black shale members display noticeable fluctuations and generally covary (Fig. 10). The Middle Bakken shows characteristic enrichments over the shales in Ca, Mg and Sr (carbonate proxies) and Mn (oxic–anoxic proxy), and depletions in all reducing condition proxies.

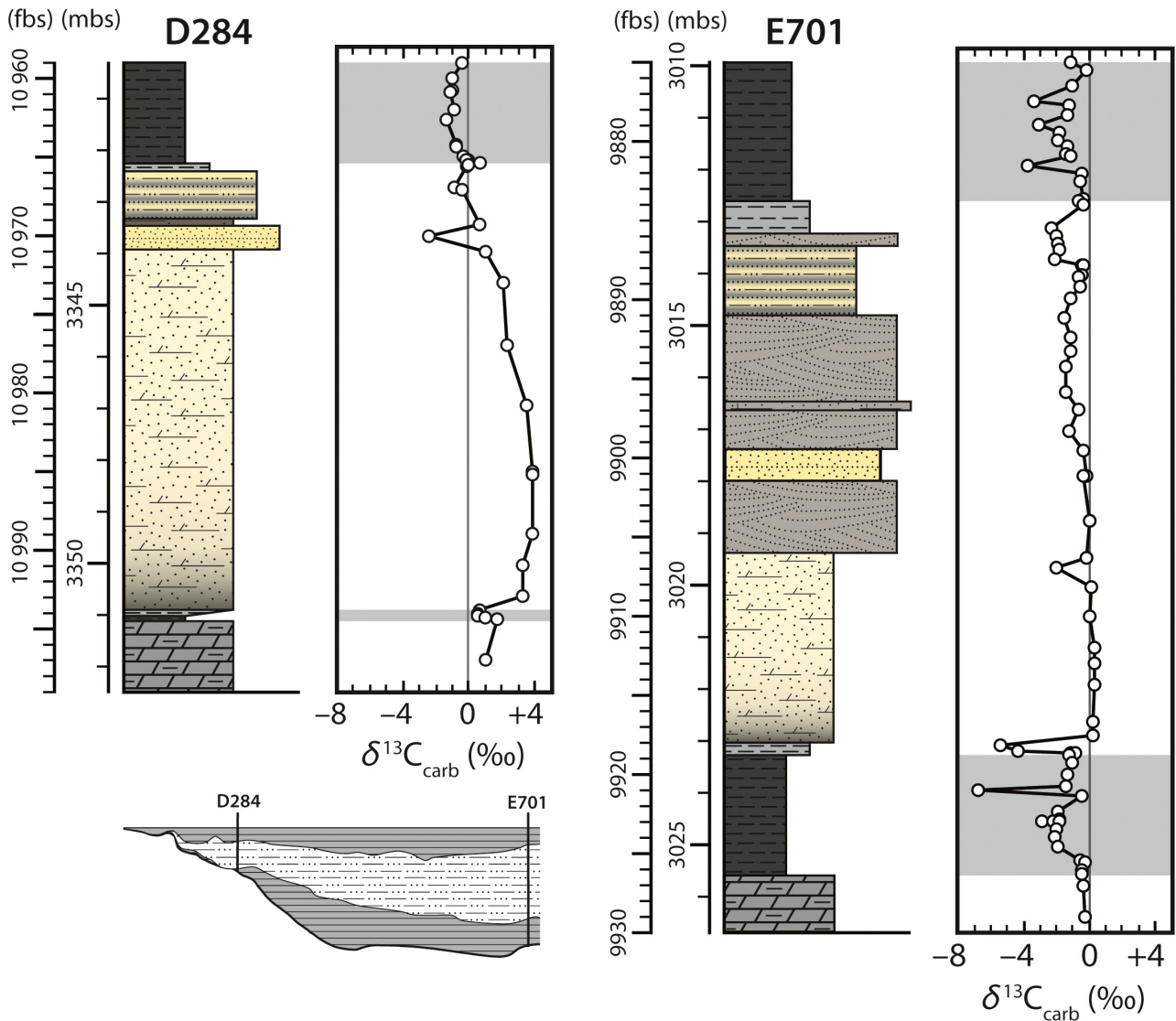


Fig. 8. Carbon isotope stratigraphy through the Bakken Formation. $\delta^{13}\text{C}_{\text{carb}}$ (‰) plotted against lithofacies stratigraphic columns for basin-marginal core D284 (left) and basin-central core E701 (right). Relative core positions displayed in inset basin cross-section (lower-left). Grey underlain boxes mark samples from black shale members. Dark grey vertical lines drawn at $\delta^{13}\text{C} = 0\text{‰}$ for reference. fbs, feet below surface; mbs, metres below surface.

The bulk geochemical data for each lithology were subjected to principal component analyses (PCA) to capture patterns of multivariate covariation in orthogonal composite variables. The first and second components (PC1 and PC2) accounted for 50 to 55% of the total observed variance (Fig. 11), whereas PC3 explains <5% of the variance. The variable loadings on these axes, represented by radiating arrows, identify four general groups of covariation for black shale data (Fig. 11A): carbonate, detrital and redox proxy groups, as well as Si. Opposing directions of loadings suggest inverse relationships for

relative enrichments. The loading for $\delta^{13}\text{C}$ shows the greatest shared variance with the detrital quadrant, which is negatively correlated with redox and silica loadings. Ninety five percent (95%) probability ellipses were calculated and overlain to show score distribution by core (Fig. 11B) and unit (Fig. 11C). The Middle Bakken PCA (Fig. 11D) shows the $\delta^{13}\text{C}$ loading covarying positively with reducing proxies. Plots with probability ellipses were similarly prepared by core (Fig. 11E) and lithofacies (Fig. 11F).

Bivariate plots and tests of correlation were performed to measure the relationship of

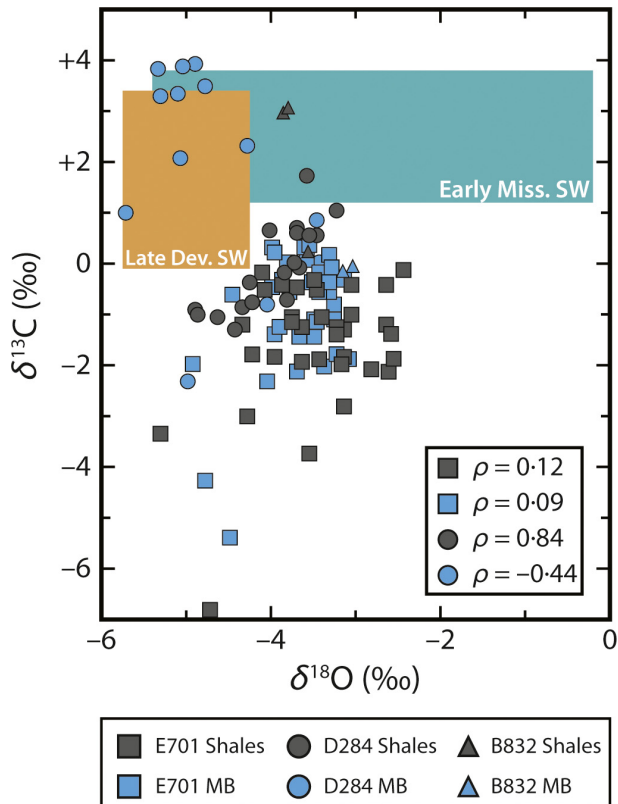


Fig. 9. Isotopic cross-plot for Bakken $\delta^{13}\text{C}_{\text{carb}}$ and $\delta^{18}\text{O}_{\text{carb}}$. Underlain boxes correspond to the estimated seawater (SW) isotopic composition range throughout the Late Devonian (van Geldern *et al.*, 2006) and Early Mississippian (Mii *et al.*, 1999) measured from brachiopods. Spearman's rank correlation (ρ) calculated for each of the study cores and members are shown in the inset.

carbonate isotopic data against bulk-rock elemental and mineralogical composition (Fig. 12; Table 4). Spearman's rank correlation coefficients and Pearson's r^2 values calculated for black shales suggest that $\delta^{13}\text{C}_{\text{carb}}$ significantly ($P < 0.05$) positively correlates with relative dolomite abundance (wt.% dolomite/wt.% carbonate), Mn/Sr (a carbonate recrystallization proxy which can be amplified by Mn remobilization in low oxygen conditions) and Zr/Al (a detrital proxy), and negatively correlates with TOC, Mo/Al and U/Al. The same calculations for the Middle Bakken show significant positive correlation of $\delta^{18}\text{O}_{\text{carb}}$ with relative dolomite abundance, $\delta^{13}\text{C}_{\text{carb}}$ with total clay, and negative correlations between $\delta^{13}\text{C}_{\text{carb}}$ and $\delta^{18}\text{O}$, quartz wt.%, dolomite, Mg/Ca and Mn/Sr (Fig. 12).

DISCUSSION

Bakken black shale redox conditions

The rate of authigenic carbonate precipitation is dependent on the level of supersaturation with respect to CaCO_3 in pore fluid. Common ancillary conditions to this process include a localized source of dissolved carbonate and sufficient dysoxia to prevent aerobic oxidation of organic matter from generating acids which lower the CaCO_3 saturation state. As such, modern sites of shallow carbonate authigenesis – for example, the Black Sea (Peckmann *et al.*, 2001) or Amazon mud belts (Aller & Blair, 2006) – feature reducing environments, steady influxes of organic carbon or methane and productive communities of microbes which anaerobically oxidize the reduced carbon and generate porewater alkalinity. When seeking a deep-time repository for authigenic carbonate, sedimentary units which were deposited under comparable redox conditions represent a promising candidate.

The Bakken Formation certainly meets the criterion for organic-rich sediments: more than 600 compiled TOC analyses from the black shale members (Table 1) average 10 wt.% and range up to 25%. This richness is likely due to a combination of elevated primary productivity driven by nutrient upwelling (Caplan & Bustin, 1998; Smith & Bustin, 1998) and increased preservation afforded by rapid delivery of organic matter (OM) to the sea floor in a shallow anoxic basin (Scott *et al.*, 2017). Water-column productivity in the Williston Basin also accounts for large silica enrichments in the black shales (Figs 7 and 11A) which suggest blooms of radiolarian zooplankton (Egenhoff & Fishman, 2013). There are no perfect modern analogues for a productive shallow seaway, but nutrient discharge from the Amazon River supports a massive planktonic community, of which *ca* 30% C_{org} is remineralized as authigenic cements (Zhu *et al.*, 2002; Aller & Blair, 2006). Aller & Blair (2006) attribute the high rates of carbonate authigenesis to dynamic sedimentary reworking overlying an active bacterial community sustained by rapid OM burial rates. Based on this analogue, the Bakken may have initially deposited higher levels of C_{org} than model estimates (Smith & Bustin, 1998) if a comparable fraction was remineralized as $\delta^{13}\text{C}$ -depleted authigenic cements.

An additional factor for modern carbonate authigenesis is dysoxic to anoxic settings. Persistent anoxia in the Bakken black shales is

Table 2. Bulk stable isotopic data from Bakken core samples: Upper Bakken black shale, UBS; Middle Bakken siltstone to sandstone, MB; Lower Bakken black shale, LBS.

Core Number	Sample depth (fbs)	Sample depth (mbs)	Unit	Lithology	$\delta^{13}\text{C}$ (‰)	$\delta^{18}\text{O}$ (‰)
E701	9875-00	3009-94	UBS	Black shale	-1.1032	-3.3837
E701	9875-50	3010-09	UBS	Black shale	-0.1444	-2.4166
E701	9876-50	3010-39	UBS	Black shale	-1.0701	-3.7509
E701	9877-50	3010-70	UBS	Black shale	-3.3954	-5.3128
E701	9877-70	3010-76	UBS	Black shale	-1.2562	-4.3387
E701	9878-30	3010-94	UBS	Black shale	-1.2887	-3.6197
E701	9879-00	3011-16	UBS	Black shale	-3.0446	-4.2740
E701	9879-50	3011-31	UBS	Black shale	-1.8270	-4.2245
E701	9880-00	3011-46	UBS	Black shale	-1.8914	-3.9588
E701	9880-30	3011-55	UBS	Black shale	-1.3029	-3.2065
E701	9880-80	3011-70	UBS	Black shale	-1.4162	-3.2235
E701	9881-00	3011-77	UBS	Black shale	-1.1731	-3.7517
E701	9881-50	3011-92	UBS	Black shale	-3.7860	-3.5337
E701	9882-00	3012-07	UBS	Black shale	-0.4296	-3.0353
E701	9882-50	3012-22	UBS	Black shale	-0.5489	-3.4447
E701	9883-60	3012-56	UBS	Black shale	-0.3710	-3.4848
E701	9883-80	3012-62	MB	Carb. wackestone	-0.6114	-3.3086
E701	9884-00	3012-68	MB	Carb. wackestone	-0.3676	-3.1184
E701	9885-50	3013-14	MB	Carb. wackestone	-2.3416	-4.0537
E701	9886-00	3013-29	MB	Sandstone	-2.0618	-3.3741
E701	9886-50	3013-44	MB	Silt-sandstone	-1.9013	-3.0680
E701	9886-90	3013-56	MB	Silt-sandstone	-1.8240	-3.2076
E701	9887-50	3013-75	MB	Silt-sandstone	-2.1534	-3.7040
E701	9887-90	3013-87	MB	Silt-sandstone	-0.5021	-3.9934
E701	9887-90	3013-87	MB	Silt-sandstone	-0.3571	-3.8702
E701	9888-50	3014-05	MB	Silt-sandstone	-0.4568	-3.8538
E701	9888-60	3014-08	MB	Silt-sandstone	-0.6213	-3.7836
E701	9889-15	3014-25	MB	Silt-sandstone	-0.5985	-3.4179
E701	9890-00	3014-51	MB	Silt-sandstone	-1.1404	-3.2631
E701	9891-20	3014-87	MB	Sandstone	-1.4957	-3.4788
E701	9892-40	3015-24	MB	Sandstone	-1.1255	-3.4694
E701	9893-30	3015-51	MB	Sandstone	-1.1271	-3.4991
E701	9894-30	3015-82	MB	Sandstone	-1.4565	-3.6478
E701	9895-90	3016-31	MB	Sandstone	-1.4475	-3.9472
E701	9897-00	3016-64	MB	Sandstone	-0.6513	-4.4442
E701	9898-30	3017-04	MB	Sandstone	-1.2756	-3.8837
E701	9899-60	3017-43	MB	Sandstone	-0.4097	-3.3156
E701	9901-10	3017-89	MB	Sandstone	-0.1328	-3.2851
E701	9901-10	3017-89	MB	Sandstone	-0.3839	-3.5148
E701	9904-00	3018-78	MB	Sandstone	0.0336	-3.5666
E701	9906-30	3019-48	MB	Siltstone	-0.1931	-3.4177
E701	9906-90	3019-66	MB	Siltstone	-2.0365	-4.9257
E701	9908-20	3020-06	MB	Siltstone	0.1495	-3.3158
E701	9910-00	3020-60	MB	Siltstone	-0.0073	-3.8021
E701	9912-00	3021-21	MB	Siltstone	0.2828	-3.6029
E701	9913-00	3021-52	MB	Siltstone	0.3358	-3.5398
E701	9914-30	3021-92	MB	Siltstone	0.2932	-3.9924
E701	9916-70	3022-65	MB	Siltstone	0.2590	-3.9843
E701	9917-50	3022-89	MB	Siltstone	0.2073	-3.9613
E701	9918-20	3023-10	MB	Carb. wackestone	-5.4552	-4.4768
E701	9918-50	3023-20	MB	Carb. wackestone	-4.3150	-4.7695
E701	9918-60	3023-23	MB	Carb. wackestone	-1.1732	-3.4447
E701	9918-70	3023-26	MB	Carb. wackestone	-0.8201	-3.2526
E701	9918-80	3023-29	LBS	Black shale	-1.2484	-2.6250
E701	9919-30	3023-44	LBS	Black shale	-1.0403	-3.0343
E701	9920-00	3023-65	LBS	Black shale	-1.3526	-3.1244

Table 2. (continued)

Core Number	Sample depth (fbs)	Sample depth (mbs)	Unit	Lithology	$\delta^{13}\text{C}$ (‰)	$\delta^{18}\text{O}$ (‰)
E701	9920.70	3023.87	LBS	Black shale	-1.3874	-2.5788
E701	9921.00	3023.96	LBS	Black shale	-6.8274	-4.7250
E701	9921.40	3024.08	LBS	Black shale	-0.4576	-2.6232
E701	9922.30	3024.35	LBS	Black shale	-1.9150	-3.4190
E701	9922.80	3024.51	LBS	Black shale	-1.8646	-3.1433
E701	9922.90	3024.54	LBS	Black shale	-2.8525	-3.1293
E701	9923.00	3024.57	LBS	Black shale	-2.1832	-2.6049
E701	9923.00	3024.57	LBS	Black shale	-1.8686	-2.5415
E701	9923.50	3024.72	LBS	Black shale	-2.0063	-3.1622
E701	9924.00	3024.87	LBS	Black shale	-2.1034	-2.7982
E701	9924.50	3025.02	LBS	Black shale	-1.9408	-3.6220
E701	9925.40	3025.30	LBS	Black shale	-0.5379	-4.0764
E701	9925.60	3025.36	LBS	Black shale	-0.2260	-4.1135
E701	9926.00	3025.48	LBS	Black shale	-0.4518	-3.8619
E701	9926.30	3025.57	LBS	Black shale	-0.4855	-3.6902
E701	9927.00	3025.79	Three Forks	Dolostone	-0.3729	-4.1735
E701	9929.00	3026.40	Three Forks	Dolostone	-0.2596	-3.7073
D284	10959.00	3340.34	UBS	Black shale	-0.4221	-4.2594
D284	10960.00	3340.65	UBS	Black shale	-0.9443	-4.8973
D284	10960.80	3340.89	UBS	Black shale	-1.0483	-4.8659
D284	10960.90	3340.92	UBS	Black shale	-1.0681	-4.6211
D284	10962.00	3341.26	UBS	Black shale	-0.9055	-4.3367
D284	10962.60	3341.44	UBS	Black shale	-1.3057	-4.4284
D284	10964.20	3341.93	UBS	Black shale	-0.7867	-4.2118
D284	10964.30	3341.96	UBS	Black shale	-0.7600	-3.7955
D284	10965.20	3342.23	UBS	Black shale	-0.2050	-3.8352
D284	10965.25	3342.25	UBS	Black shale	-0.0338	-3.7341
D284	10965.30	3342.26	UBS	Black shale	-0.0882	-3.6756
D284	10965.35	3342.28	UBS	Black shale	0.6777	-3.7047
D284	10965.50	3342.33	MB	Carb. wackestone	-0.0080	-3.4377
D284	10967.00	3342.78	MB	Sandstone	-0.8601	-4.0438
D284	10967.10	3342.81	MB	Sandstone	-0.3729	-3.4978
D284	10969.35	3343.50	MB	Siltstone	0.8312	-3.4456
D284	10970.00	3343.70	MB	Sandstone	-2.3697	-4.9889
D284	10971.00	3344.00	MB	Siltstone	0.9728	-5.7114
D284	10973.00	3344.61	MB	Siltstone	2.0359	-5.0749
D284	10977.00	3345.83	MB	Siltstone	2.2769	-4.2727
D284	10980.80	3346.99	MB	Siltstone	3.4487	-4.7658
D284	10985.00	3348.27	MB	Siltstone	3.8757	-4.8828
D284	10985.10	3348.30	MB	Siltstone	3.8292	-5.0453
D284	10989.00	3349.49	MB	Siltstone	3.8184	-5.3290
D284	10991.00	3350.10	MB	Siltstone	3.2466	-5.3118
D284	10993.00	3350.71	MB	Siltstone	3.2872	-5.1098
D284	10993.80	3350.95	LBS	Black shale	0.6215	-4.0161
D284	10994.00	3351.01	LBS	Black shale	0.5878	-3.6920
D284	10994.10	3351.04	LBS	Black shale	0.5382	-3.4508
D284	10994.20	3351.07	LBS	Black shale	0.5281	-3.5426
D284	10994.30	3351.10	LBS	Black shale	0.9986	-3.2088
D284	10994.40	3351.13	LBS	Black shale	1.7020	-3.5775
D284	10997.00	3351.93	Three Forks	Dolostone	1.0200	-3.7701
B832	10356.40	3156.67	UBS	Black shale	0.3170	-3.6102
B832	10356.50	3156.70	UBS	Black shale	0.2152	-3.5859
B832	10361.00	3158.07	MB	Siltstone	-0.0808	-3.1565
B832	10361.10	3158.10	MB	Siltstone	-0.1544	-3.0573
B832	10372.60	3161.61	LBS	Black shale	2.9870	-3.8708
B832	10372.70	3161.64	LBS	Black shale	3.0802	-3.7955

Table 3. Average Al-normalized elemental composition of the Bakken Formation members relative to an average shale (Wedepohl, 1971); $n_{\text{UBS}} = 40$, $n_{\text{MB}} = 66$ and $n_{\text{LBS}} = 26$. Lower Bakken black shale, LBS; Middle Bakken siltstone to sandstone, MB; Upper Bakken black shale, UBS.

Element	UBS	MB	LBS	Average shale
Al (wt.%)	3.56	3.11	5.01	8.84
Si/Al	8.52	6.95	5.19	3.12
K/Al	0.89	0.84	0.86	0.34
Ca/Al	0.63	6.31	0.72	0.18
Mg/Al	0.33	0.73	0.26	0.18
Fe/Al	1.27	0.67	0.88	0.55
S/Al	0.93	0.30	0.52	0.03
As/Al*	2.26	0.52	1.57	0.11
Cr/Al*	2.60	1.98	2.06	1.02
Cu/Al*	3.11	0.27	1.60	0.51
Mn/Al*	2.58	16.10	4.12	9.62
Mo/Al*	8.73	0.40	6.43	0.03
Ni/Al*	7.50	1.91	4.81	0.77
P/Al*	33.57	0.00	26.53	7.92
Pb/Al*	1.17	0.61	0.81	0.23
Rb/Al*	3.19	2.55	3.20	1.58
Sr/Al*	1.56	5.25	1.68	3.39
Th/Al*	0.25	0.35	0.20	0.14
Ti/Al*	62.70	66.00	60.40	52.90
U/Al*	1.80	0.06	1.55	0.04
V/Al*	27.00	4.09	14.60	1.47
Zn/Al*	99.60	0.96	37.70	0.01
Zr/Al*	3.28	8.28	2.17	1.81

* Values $\times 1000$.

supported by the high levels of preserved TOC and trace metals (Table 3). However, the black shales' chemostratigraphic data indicate fluctuations in the redox state of the Williston Basin: most redox proxies share minima towards the base of the Lower Bakken (Fig. 10), suggesting that anoxic conditions did not set in immediately during the initial marine transgression. Multiple redox proxy minima in E701 (Fig. 10) demonstrate that even in the deeper basin anoxic conditions were not constant. These observations are consistent with previous interpretations of Bakken trace fossils and geochemistry which hypothesized low-oxygen but not anoxic conditions for intervals in the Bakken black shales (Egenhoff & Fishman, 2013; Fishman *et al.*, 2015; *cf.* comment by Schieber, 2014). An alternative hypothesis posits that in seasonal or climate-driven oxic/anoxic to euxinic fluctuations Late Devonian ichnofauna could persist (Boyer *et al.*, 2011), corroborated by ichnofauna recognized elsewhere in the Bakken

(Angulo & Buatois, 2012). In this model, the chemocline may have shoaled into the photic zone in response to the build-up of bottom-water H_2S (Algeo & Tribovillard, 2009; Scott *et al.*, 2017; Aderoju & Bend, 2018). The position of the chemocline would therefore be subject to similar controls as SRM activity: organic carbon and sediment accumulation rate, O_2 , SO_4^{2-} and the inhibitory build-up of H_2S .

A shoaling chemocline allows for a dynamic redox history in which fluctuations in euxinia are potentially independent of the Williston Basin's seawater circulation and base-level trends. The TOC and redox proxy minima in the black shale members (Fig. 10) could therefore represent intermittent redox instability in the position of the chemocline, while protracted shoaling above the basin centre explains the greater redox proxy enrichments in core E701 than D284 (Fig. 11B). Supporting evidence for periodic euxinia in the Williston Basin includes 'hyper-enrichments' of Zn and V (Fig. 10; Table 3; Scott *et al.*, 2017), as well as pyrite and sphalerite enrichments (Table 1) which occur as macroscopic blebs and $>500 \mu\text{m}$ framboids to polyframboids (Fig. 6D). In the Black Sea, a modern analogue for epicontinental photic-zone euxinia, sea floor methane seeps are rapidly anaerobically oxidized to form isotopically depleted aragonite deposits (Peckmann *et al.*, 2001). It is therefore reasonable to hypothesize that the redox conditions and high organic matter burial rates in the Williston Basin supported active communities of SRM which could effectively remineralize organic carbon and induce authigenic carbonate formation.

Bakken authigenic carbonate mass and isotopic composition

The first crucial assumption in the authigenic carbon model (Schrag *et al.*, 2013) is that the burial of authigenic carbonate is comparable to organic carbon and marine carbonate fluxes. Accurately estimating this term, however, is difficult: significant authigenic burial fluxes can manifest as subtle changes in bulk geochemistry, and studies targeting pre-Jurassic periods lack the deep sea sedimentary record which is an important locus of authigenic carbonate burial in the modern ocean (Mitnick *et al.*, 2018; Bradbury & Turchyn, 2019). For this reason, calculating the global authigenic carbon sink from Palaeozoic epicontinental records may represent only a conservative estimate.

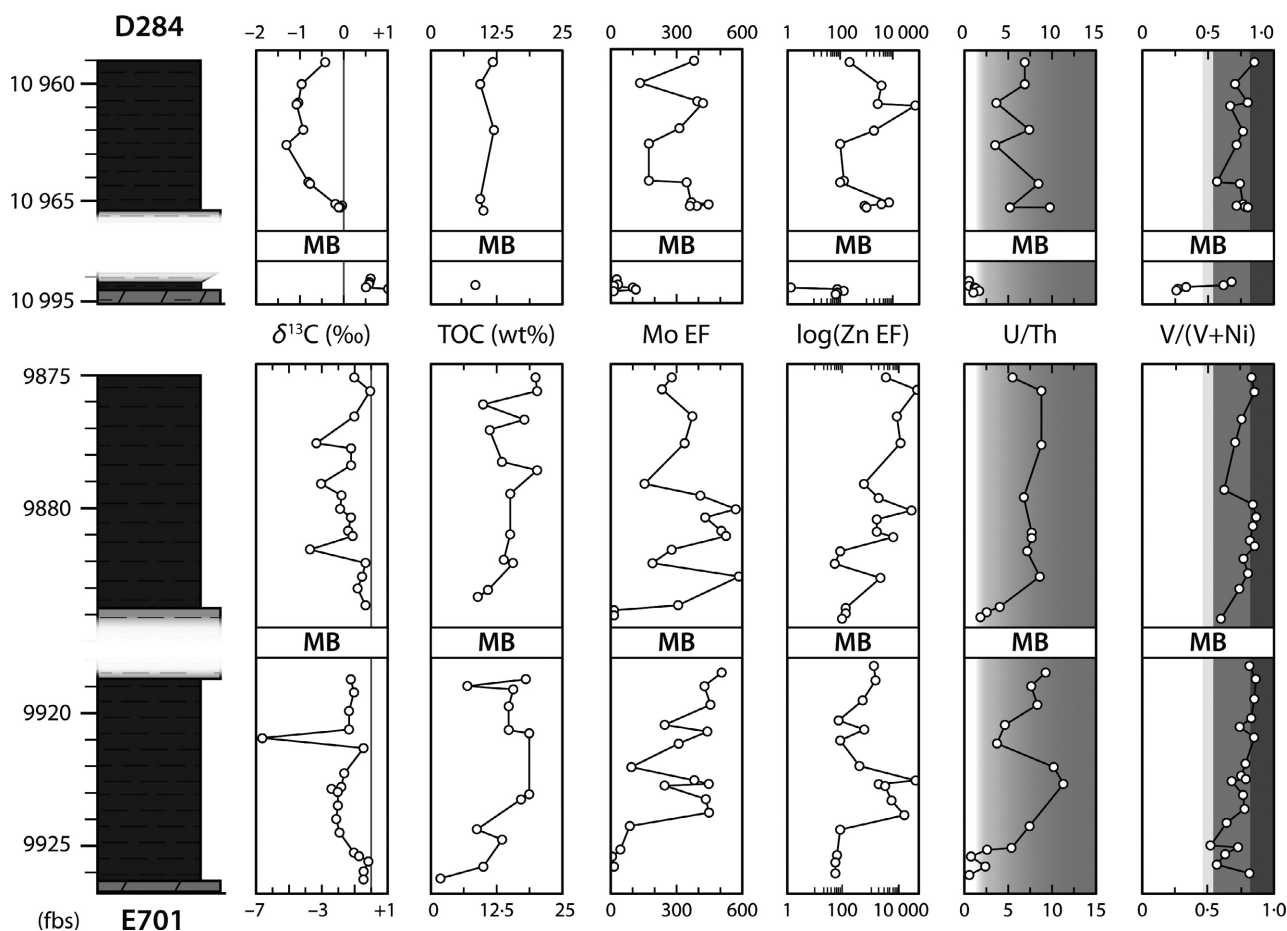


Fig. 10. Redox geochemical stratigraphy within the Upper and Lower Black Shale members. Plots for basin–marginal core D284 on top, and basin–central E701 at the bottom. The geochemical proxies include $\delta^{13}\text{C}_{\text{carb}}$ (‰) and total organic carbon (TOC) wt.%; log-transformed enrichment factors (EF) for Mo and Zn (Table S1) calculated as $(X/Al)_{\text{sample}}/(X/Al)_{\text{average shale}}$ with average shale values from Wedepohl (1971) in Table 3; and qualitative redox proxies U/Th and V/(V + Ni). Note that each core's $\delta^{13}\text{C}$ is plotted on different axes to emphasize stratigraphic variability. The dark grey underlay in the U/Th plot corresponds to interpreted anoxia (Jones & Manning, 1994), while the light grey, grey and dark grey boxes in V/(V + Ni) depict enrichment levels corresponding to dysoxia, anoxia and euxinia (Hatch & Leventhal, 1992). fbs, feet below surface; MB, Middle Bakken member. Metric depths as in Fig. 8.

Compiled Bakken XRD measurements (USGS CRC, 2016) show considerable detrital/authigenic carbonate mass for a siliciclastic unit, averaging 10.3 wt.% carbonate in the Upper Bakken Black Shale, 47.6 wt.% in the Middle Bakken and 6.76 wt.% in the Lower Bakken Black Shale (Table 1). Assuming that these averages are representative of the entire Bakken Formation, a first-order approximation of the total carbon burial may be calculated. Average unit thicknesses (UBS = 2 m, MB = 13 m, LBS = 3 m; Smith *et al.*, 1995) are assumed to extend throughout a basin with area $3.44 \times 10^5 \text{ km}^2$. Each unit's density is estimated from USGS CRC compiled data (UBS = 2727 kg/m^3 ,

MB = 2738 kg/m^3 , LBS = 2764 kg/m^3). From these metrics and the average TOC wt.% (Table 1), the total organic carbon burial in the Bakken Formation is calculated to be 4.34×10^{16} moles (the black shale members comprising 3.84×10^{16} mol organic C). Following the same steps with the remainder Bakken mineral mass and average calcite and dolomite composition from Table 1 yields an estimate for the Bakken carbonate–carbon burial term of 6.51×10^{16} mol C (3.72×10^{15} mol C in the black shales).

It must be reiterated that the carbonate mass cited above comprises both primary and secondary components, i.e. detrital or biogenic

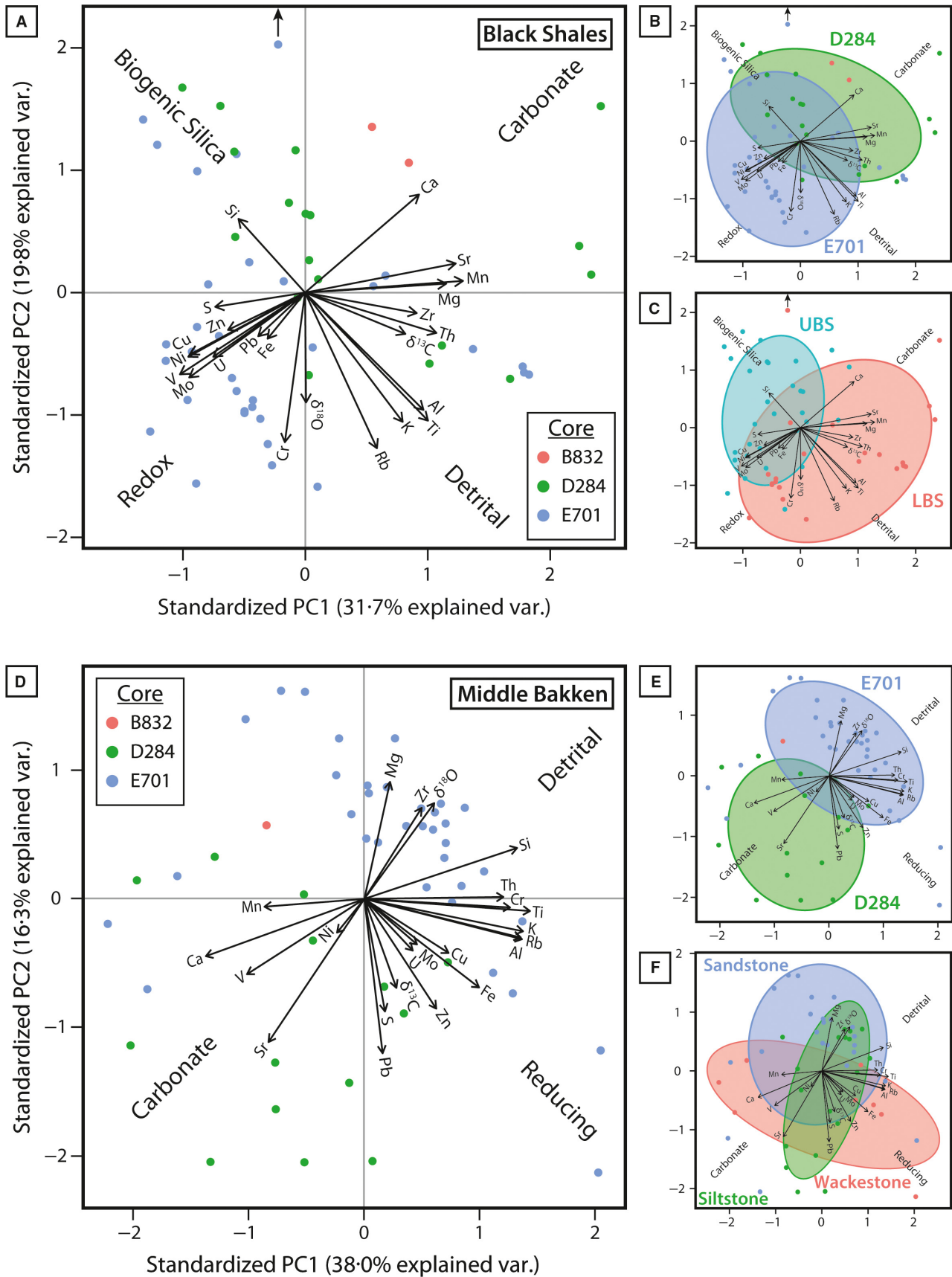


Fig. 11. Principal component analyses (PCA) biplots for elemental and isotopic data. Methods described in the *Results* section. (A) Black shales geochemical dataset PCA, with scores colour-coded by core number (inset). The variable loadings covary into four main proxy directions, labelled by quadrant. Note the shifted E701 outlier score at the top. (B) Black shales PCA with 95% probability ellipses calculated by core number. (C) Black shales PCA with 95% probability ellipses calculated by member. (D) Middle Bakken geochemical dataset PCA, with variable loadings covarying in three main proxy directions. (E) Middle Bakken PCA with 95% probability ellipses calculated by core number. (F) Middle Bakken PCA with 95% probability ellipses calculated by lithofacies.

marine carbonate as well as all diagenetic phases. This distinction may not be necessary because, from a global carbon-isotope mass-balance perspective, distinguishing authigenic carbonate from primary is irrelevant so long as the bulk mass and isotopic composition are well-constrained. The burial of a known mass of carbonate with a known $\delta^{13}\text{C}_{\text{bulk}}$ will impact $\delta^{13}\text{C}_{\text{DIC}}$ at a calculable magnitude, regardless of the exact admixtures of primary and authigenic carbonate. However, a major caveat to this assumption is that the authigenic carbonate must form relatively early, such that the sedimentary pore fluids

remain in diffusive or advective contact with co-eval seawater. Once sediments become sealed off from exchange with seawater, continuing remineralization of buried organic carbon will no longer impact $\delta^{13}\text{C}_{\text{DIC}}$. In this context, ‘authigenic’ cannot be used synonymously with ‘diagenetic’ because the latter term broadly comprises all secondary phases, including late-stage cements formed in isolation from seawater during deeper burial. Conversely, carbonate cements which form through interaction with meteoric fluids in subaerial-shallow sedimentary environments can exert a similar impact to $\delta^{13}\text{C}_{\text{DIC}}$ as the

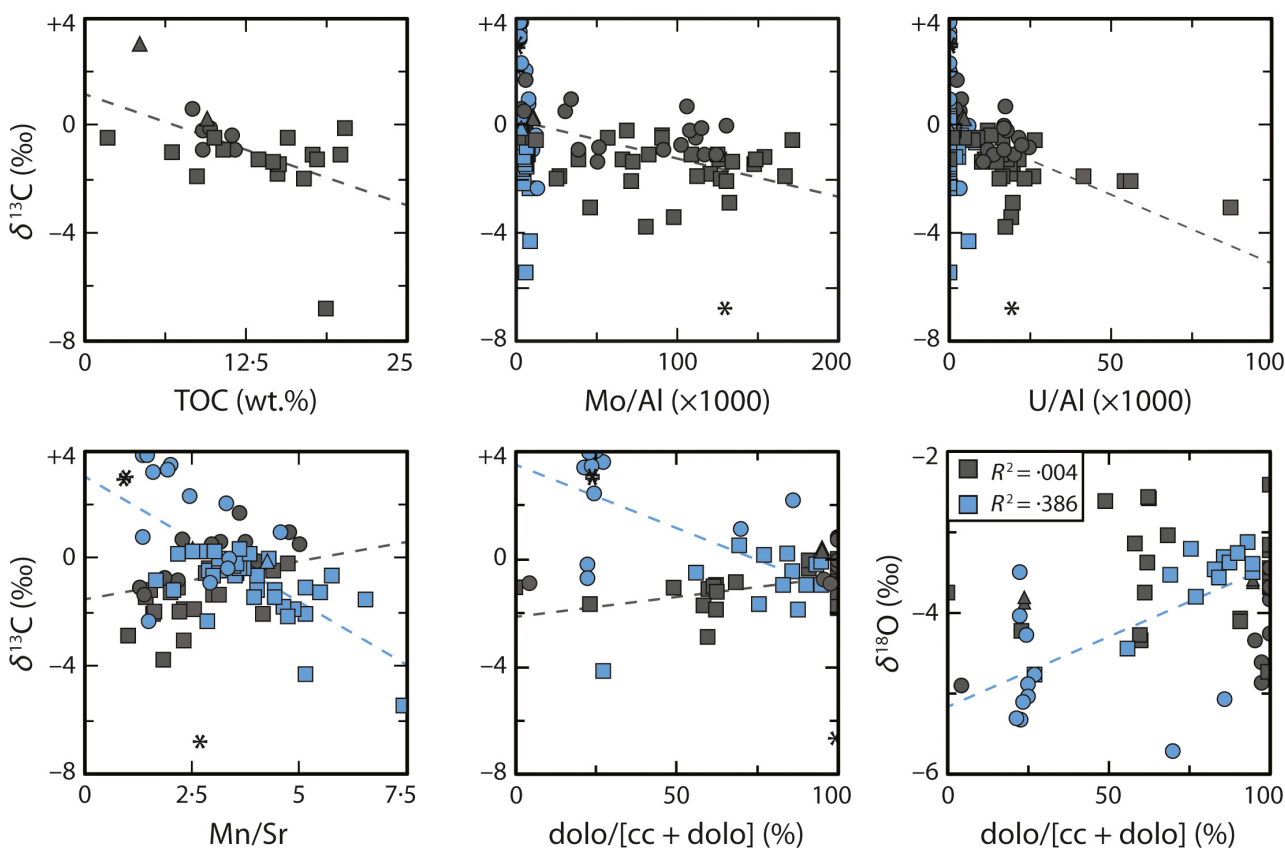


Fig. 12. Cross-plots for bulk geochemical composition data. Plots use same symbols as in legend of Fig. 9. Dashed linear regression lines are plotted where the correlation is significant, as listed in Table 3 or inset legend. Asterisks represent three black shale elemental and mineralogical outliers which were excluded from the correlation calculations.

Table 4. Spearman's correlation coefficients, *P*-value significance, and *R*² values for relationships between $\delta^{13}\text{C}_{\text{carb}}$ and mineralogical and elemental composition data. Statistically significant relationships are indicated with bold (*P* < 0.05) or bold and italicized text (*P* < 0.01).

	Spearman's ρ	<i>P</i> -value	<i>r</i> ²	<i>n</i>
Black shales $\delta^{13}\text{C}$				
$\delta^{18}\text{O}$ (‰)	-0.0780	0.5824	0.0044	52
TOC (wt.%)	-0.5181	0.0067	0.3334	26
Quartz (wt.%)	-0.1470	0.4301	0.0468	31
Total clay (wt.%)	0.0567	0.7619	0.0125	31
Total carbonate (wt.%)	0.1391	0.4555	0.0764	31
Dolomite/(calcite + dolomite)	0.5891	0.0101	0.2331	19
Mg/Ca	-0.2889	0.0635	0.0901	42
Mn/Sr	0.5870	0.0001	0.3205	37
Mo/Al	-0.4257	0.0017	0.1630	52
U/Al	-0.6223	0.0000	0.3419	51
Zr/Al	0.4627	0.0006	0.1320	52
Middle Bakken $\delta^{13}\text{C}$				
$\delta^{18}\text{O}$ (‰)	-0.3630	0.0104	0.3560	49
TOC (wt.%)	-	-	-	-
Quartz (wt.%)	-0.4216	0.0451	0.3576	23
Total clay (wt.%)	0.6240	0.0015	0.6671	23
Total carbonate (wt.%)	0.0791	0.7198	0.0024	23
Dolomite/(calcite + dolomite)	-0.5240	0.0103	0.4967	23
Mg/Ca	-0.3278	0.0319	0.2170	43
Mn/Sr	-0.5948	0.0000	0.4579	49
Mo/Al	-0.1604	0.2815	0.0578	47
U/Al	-	-	-	-
Zr/Al	-0.0531	0.7231	0.0555	47

'marine' authigenic carbonate flux envisioned by Schrag *et al.* (2013), provided that the meteoric cements are not subsequently chemically weathered (e.g. Dyer *et al.*, 2015).

Observations from thin sections support the existence of diverse carbonate phases in the Bakken Formation (Fig. 6). Detrital calcite and dolomite grains were distinguished as weathered, irregular subhedral to anhedral crystals, and seem to be predominantly concentrated in silt laminae (Fig. 6A). In the clay matrix, dolomite occurs as randomly oriented disseminated subhedral to euhedral rhomb crystals interpreted to represent diagenetic precipitation. The rarity of fracture-fill calcite cements and veins in hand sample and thin section suggest that late-stage diagenetic phases are relatively minor constituents. Given the fine scale of the carbonate crystals ($\leq 10 \mu\text{m}$) it is often difficult to distinguish detrital grains from cements, an issue which is compounded by the observation that authigenic dolomite commonly occurs as overgrowths on detrital grains and calcite cements appear to incorporate primary grains into their crystals (Fishman *et al.*, 2015).

Without a reliable petrographic technique to distinguish primary/detrital grains from diagenetic phases, micron-scale elemental and isotopic data from Bakken carbonates must instead constrain the relative timing of their precipitation. For the purposes of developing a basin-scale carbonate mass balance, if most calcite and dolomite mass represents early precipitation formed in connection with seawater, then the net effect of its burial on $\delta^{13}\text{C}_{\text{DIC}}$ can be modelled. Previous reconstructions of the Bakken's diagenetic history (Fishman *et al.*, 2015; Brennan, 2016) propose that calcite and dolomite cementation took place relatively early, noting that calcite cement formed in laminae and microfossils prior to post-depositional compaction. Microscale $\delta^{18}\text{O}$ composition of cements by SIMS and fluid inclusion microthermometry suggest that Middle Bakken calcite cements represent syn-sedimentary features which began to precipitate from seawater near the sediment-water interface (see link to data in the *Acknowledgements*; Brodie *et al.*, 2018). Furthermore, microscale measurements of Middle Bakken dolomite crystals demonstrate

that the inner zones feature a narrow range of $\delta^{18}\text{O}$ and a wide range of $\delta^{13}\text{C}$ throughout the Williston Basin, suggesting early precipitation from seawater with local sources of ^{13}C -depleted DIC (for example, SRM), whereas progressive trends in oxygen in the outermost zones are indicative of late-stage fluid migration and precipitation during burial diagenesis (Denny *et al.*, 2019).

Based on the above lines of evidence, it is hypothesized that early carbonate precipitates derived from a mixture of seawater DIC and respired organic matter represent the more significant diagenetic carbonate mass. Furthermore, because the current study's sampling strategy in the black shale members generally avoided visible carbonate veins and significant silt laminae, the isotopic analyses should better reflect the randomly oriented, inferred authigenic dolomite rhombs observed in thin section (Fig. 6). The assumption is then made that the majority of the combined detrital/authigenic mass represents carbonate formed in connection to the basin's seawater, rather than later burial phases produced in isolation from the overlying exogenic carbon reservoir.

The second crucial assumption made in the authigenic carbon model is that the burial term is isotopically depleted relative to seawater dissolved inorganic carbon ($\delta^{13}\text{C}_{\text{DIC}}$), represented by the isotopic offset term ε_{AC} (Schrag *et al.*, 2013). This value can vary significantly when authigenic carbonate is an admixture of multiple carbon sources, for example isotopically enriched seawater DIC and isotopically depleted HCO_3^- sourced from the oxidation of organic matter or methane. The initial model's estimated $\varepsilon_{\text{AC}} = 15$ to 20‰ seems to derive from empirical data from Amazon shelf sediments which feature diagenetic carbonates within a range of -19 to -15‰ (Zhu *et al.*, 2002). The bulk carbonate $\delta^{13}\text{C}$ and ε_{AC} may thus be teased apart through mass balance:

$$\delta^{13}\text{C}_{\text{bulk}} = X_{\text{org}}(\delta^{13}\text{C}_{\text{DIC}} - \varepsilon_{\text{org}}) + (1 - X_{\text{org}})(\delta^{13}\text{C}_{\text{DIC}} - \varepsilon_{\text{MC}}) \quad (1)$$

$$\varepsilon_{\text{AC}} = \delta^{13}\text{C}_{\text{DIC}} - \delta^{13}\text{C}_{\text{bulk}} = X_{\text{org}}\varepsilon_{\text{org}} + (1 - X_{\text{org}})\varepsilon_{\text{MC}} \quad (2)$$

where X_{org} = the fraction of bulk carbonate derived from remineralized organic carbon, ε_{org} = the isotopic offset associated with that

organic carbon source (simplified $\varepsilon_{\text{org}} \approx \varepsilon_{\text{P}} \approx 25\text{‰}$ for most photosynthetic biomass in this study) and ε_{MC} is the isotope enrichment associated with carbonate precipitation ($\varepsilon_{\text{MC}} \approx -1\text{‰}$). Solving for X_{org} :

$$X_{\text{org}} = \frac{\delta^{13}\text{C}_{\text{bulk}} - (\delta^{13}\text{C}_{\text{DIC}} - \varepsilon_{\text{MC}})}{\varepsilon_{\text{MC}} - \varepsilon_{\text{org}}} \quad (3)$$

and assuming modern $\delta^{13}\text{C}_{\text{DIC}} \approx 0\text{‰}$, the Amazonian authigenic carbonates ($\delta^{13}\text{C}_{\text{bulk}} = -19$ to -15‰) represent approximately 62 to 77% carbon sourced from remineralized C_{org} . This calculation may be modified for different reduced carbon sources: for example, $\delta^{13}\text{C}_{\text{bulk}}$ of methane-derived authigenic cements in the Black Sea ranges from -47 to -26‰ , with sampled methane yielding an isotopic composition of -68‰ (Peckmann *et al.*, 2001). Setting the fractionation term in Eq. 3 equal to the methane offset ($\varepsilon_{\text{org}} = 68\text{‰}$) predicts a methanic contribution to the sea floor carbonates of approximately 39 to 70%. Comparatively, a study of methane seep cements in the Gulf of Mexico ($\delta^{13}\text{C}_{\text{bulk}} = -38$ - 91‰) concluded that the composition reflected primarily methane and hydrocarbon sourcing (83%) with minimal seawater DIC input (Formolo *et al.*, 2004). Clearly, a 'typical' ε_{AC} can vary broadly, but as a general rule authigenic precipitates in the modern ocean have more depleted compositions which allow them to be distinguished from primary carbonates.

Applying Eq. 3 to the Bakken black shales dataset (Table 2), assuming $\varepsilon_{\text{org}} = 25\text{‰}$ and baseline $\delta^{13}\text{C}_{\text{DIC}} = +2.0\text{‰}$, yields a predicted organic contribution (X_{org}) of 18% for E701 (12 to 38%) and 12% for D284 (5 to 17%). If these admixtures represented 100% authigenic cements, their mean authigenic isotopic offset would average $\varepsilon_{\text{AC}} = 3.7\text{‰}$ for E701 (2.1 to 8.9‰) and 2.1‰ for D284 (0.3 to 3.4‰), significantly smaller than the above modern examples. These results highlight the contrast in the carbonate isotopic composition of the deeper basin-central and shallower basin-marginal core sites (e.g. Qie *et al.*, 2015). These trends could be explained by the efficiency of organic carbon remineralization, potentially in connection with the duration and intensity of euxinic conditions in tandem with a decreased relative sedimentation rate and an increased oxygen exposure time at the basin margin. Alternatively, the cements in the black shales may have been enriched by methanogenic metabolisms deeper in the burial process, similar to interpretations

from high- $\delta^{13}\text{C}$ Late Devonian shale-hosted concretions (Lash, 2018). This study finds no additional evidence in the Bakken shales to support the presence of methanogenesis in the zone of carbonate authigenesis (for example, isotopic enrichment above $\delta^{13}\text{C}_{\text{DIC}}$). The modelled organic contribution to the shallow Middle Bakken carbonate $\delta^{13}\text{C}_{\text{bulk}}$ averages 15% for E701 and 5% for D284, with mean $\epsilon_{\text{AC}} = 2.9\text{‰}$ and 0.3‰ , respectively. From these estimates it would appear that the burial of the Middle Bakken contributed to the depleted authigenic carbon sink at a comparable magnitude to the black shale members. In summary, the mean Bakken Formation $\epsilon_{\text{AC}} = 0.3$ to 3.7‰ suggests that the assumption of a significant isotopic depletion between authigenic carbonate and DIC is not valid for this unit.

Given the potential cumulative importance of disseminated authigenic carbonates in siliciclastic units and the difficulty of targeting these microscopic features for isotopic analysis, future studies will benefit from bulk mineralogical and elemental proxies for regions of low- $\delta^{13}\text{C}$ carbonate cements. By investigating correlations between isotopic and compositional data (Table 4; Figs 11 and 12), geochemical proxies were developed for environments in which remineralization of organic carbon into authigenic carbonate appears to be promoted. The results for the black shale members suggest that $\delta^{13}\text{C}_{\text{carb}}$ significantly tends towards more depleted values in environments enriched in total organic carbon, Mo/Al and U/Al, which all correlate with anoxic conditions (Fig. 12). Strong positive relations with Mn/Sr (Fig. 12) and Zr (Fig. 11A) suggest that enriched $\delta^{13}\text{C}_{\text{carb}}$ values correspond to facies recrystallizing in variably oxic–anoxic conditions with a greater influx of detrital materials. Zirconium/aluminium enrichments may correlate with silt laminae formed during high-energy storm transport, which additionally deposit carbonate grains from further up the slope that are isotopically similar to basin DIC. Therefore, the major controls on the distribution of low- $\delta^{13}\text{C}$ authigenic carbonate in the black shale facies seem to be redox conditions, organic matter burial and lithology.

Spearman rank-correlation coefficients for the shallow, carbonate-rich Middle Bakken samples suggest that $\delta^{13}\text{C}_{\text{carb}}$ is most depleted in zones of enriched $\delta^{18}\text{O}$, quartz wt.% and Mn/Sr (Table 4; Fig. 12). Quartz content here may correlate with coarser sandstones facies featuring reworked intraclasts and ooids (Fig. 6F) which

were potentially susceptible to fluid flow and diagenetic alteration. This is further supported by the positive $\delta^{13}\text{C}$ –total clay wt.% correlation, interpreted to represent deeper water clay-rich facies which are less permeable through burial and thereby avoid alteration. Correlation between carbon and oxygen stable isotopes may reflect mixing between meteoric fluids from the continental margin, rich in depleted CO_2 derived from organic carbon and rainfall-fractionated $\delta^{18}\text{O}$, with seawater in shallow sediments (e.g. Allan & Matthews, 1982; Swart & Oehlert, 2018). Alternatively, the weak relationship between dolomite fraction and carbonate $\delta^{13}\text{C}$ and $\delta^{18}\text{O}$ composition (Fig. 12) may reflect the isotopic effects of dolomitization (Denny *et al.*, 2019). Finally, the negative correlation between Mn/Sr and $\delta^{13}\text{C}_{\text{carb}}$ is interpreted to track bulk diagenetic alteration of the carbonates in intermittently anoxic pore fluids (Brand & Veizer, 1980; Banner & Hanson, 1990). Based on these proxy relationships, the major controls on burial of authigenic carbonate in generally oxic silt–sandstone facies are related to carbonate recrystallization in the meteoric/seawater mixing zone and pore fluid evolution through dolomitization.

The role of authigenic carbonate in the Hangenberg excursion

Since the $\delta^{13}\text{C}$ composition of carbonates is assumed to reflect the composition of the marine DIC (Saltzman & Thomas, 2012), the geological record of $\delta^{13}\text{C}_{\text{carb}}$ may be inverted to model the required oscillations in any one variable to drive secular trends in $\delta^{13}\text{C}_{\text{DIC}}$. This data inversion draws upon carbon isotope mass balance equations outlined in Kump & Arthur (1999) and Kurtz *et al.* (2003), with an added authigenic carbonate sink term:

$$\begin{aligned} \frac{d}{dt}(M_C\delta^{13}\text{C}_{\text{DIC}}) = & F_W\delta^{13}\text{C}_W - F_B(f_{\text{MC}}\delta^{13}\text{C}_{\text{DIC}} \\ & + f_{\text{OC}}(\delta^{13}\text{C}_{\text{DIC}} - \epsilon_P) \\ & + f_{\text{AC}}(\delta^{13}\text{C}_{\text{DIC}} - \epsilon_{\text{AC}})) \end{aligned} \quad (4)$$

in which M_C represents the mass of the ocean-atmosphere carbon reservoir, F_W = the weathering flux of carbon into the ocean, F_B = the burial flux of carbon out of the ocean, $\delta^{13}\text{C}_W$ = the isotopic composition of weathered carbon, and f_{MC} , f_{OC} and f_{AC} are fractional burial terms for marine carbonate, organic and authigenic

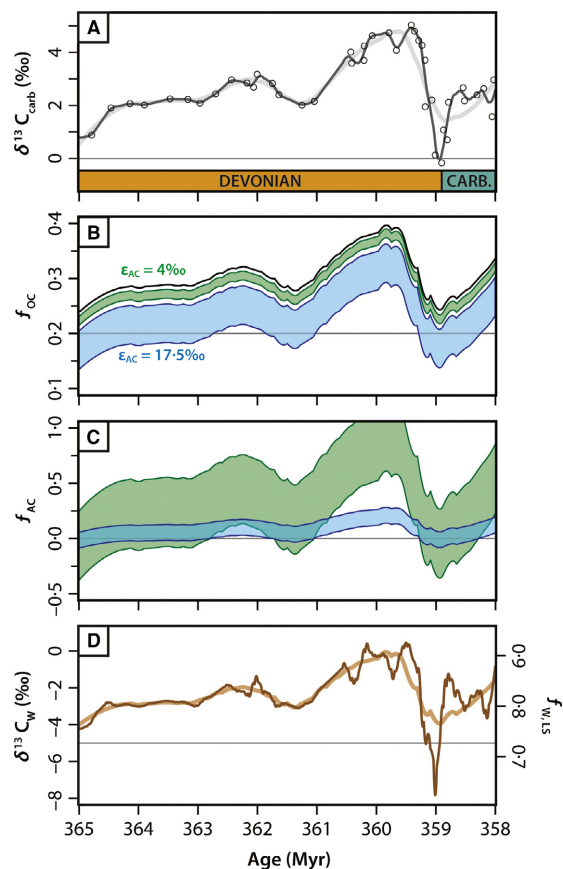


Fig. 13. Inverse box-model results for global carbon cycle forcings across the Hangenberg positive carbon-isotope excursion. Model based on equations and parameters from Kump & Arthur (1999) and Kurtz *et al.* (2003); assumed modern steady-state values for each variable are illustrated by the grey lines. (A) $\delta^{13}\text{C}_{\text{carb}}$ record across the Devonian–Carboniferous boundary interpolated from a dataset from Saltzman & Thomas (2012) plotted as black points. The record has been Loess-smoothed with spans set to 0.25 (thick light grey line) and 0.05 (thin dark grey line). (B) Modelled fractional burial of organic carbon (f_{OC}) required to drive smoothed $\delta^{13}\text{C}_{\text{carb}}$ trends in (A), assuming no authigenic carbonate burial flux (black line), or assuming an authigenic burial term of 0.05 to 0.15 where $\epsilon_{\text{AC}} = 4\text{‰}$ (green trends; after Bakken E701 data) or $\epsilon_{\text{AC}} = 17.5\text{‰}$ (blue trends; after Schrag *et al.*, 2013). (C) Modelled fractional burial of authigenic carbon (f_{AC}) required to drive smoothed $\delta^{13}\text{C}_{\text{carb}}$ trends in (A), assuming an organic burial term of 0.2 to 0.3 where $\epsilon_{\text{AC}} = 4\text{‰}$ (green trends) or $\epsilon_{\text{AC}} = 17.5\text{‰}$ (blue trends). (D) Modelled isotopic composition of riverine inputs of carbon ($\delta^{13}\text{C}_{\text{W}}$) required to drive smoothed $\delta^{13}\text{C}_{\text{carb}}$ trends in (A), assuming $f_{\text{OC}} = 0.2$ and $f_{\text{AC}} = 0.0$. The riverine input is modelled as an isotopic mixture of weathered carbonate lithologies ($+2.5\text{‰}$) and fossil organic carbon (-25‰) after Kump *et al.* (1999) and can be expressed as the fractional contribution of limestone to the carbon input ($f_{\text{W,LS}}$ on the right axis).

carbon, respectively. Equation 4 may be rearranged to:

$$\frac{d\delta^{13}\text{C}_{\text{DIC}}}{dt} = \frac{F_{\text{W}}(\delta^{13}\text{C}_{\text{W}} - \delta^{13}\text{C}_{\text{DIC}}) + F_{\text{B}}(f_{\text{OC}}\epsilon_{\text{P}} + f_{\text{AC}}\epsilon_{\text{AC}})}{M_{\text{C}}} \quad (5)$$

which assumes a well-mixed ocean and steady state with respect to mass ($F_{\text{W}} = F_{\text{B}}$; M_{C} is constant through time), but non-steady-state with respect to seawater isotopic composition. For a given carbonate–carbon isotope stack the $\delta^{13}\text{C}_{\text{DIC}}$ may be input and Eq. 4 rearranged to solve for any variable, assuming that all others remain constant. This model (Fig. 13) was run for time steps of 1 kyr with $\delta^{13}\text{C}$ data from Saltzman & Thomas (2012) and modern carbon cycle parameters from Kurtz *et al.* (2003): $M_{\text{C}} = 4.0 \times 10^{18}$ mol C, $F_{\text{W}} = F_{\text{B}} = 25 \times 10^{15}$ mol C/kyr, $\epsilon_{\text{P}} = 25\text{‰}$ and $\delta^{13}\text{C}_{\text{W}} = -5\text{‰}$. Initial parameters for authigenic carbon burial (f_{AC} and ϵ_{AC}) were estimated from this study's Bakken data and the Schrag *et al.* (2013) model assumptions.

The Hangenberg CIE (Fig. 13A) has been traditionally interpreted to result from a sharp increase in organic carbon burial rates (Caplan & Bustin, 1999; Kaiser *et al.*, 2006, 2016; Cramer *et al.*, 2008). Using the inverse model approach, the changes in f_{OC} required to drive the observed CIE can be estimated for various authigenic burial scenarios (Fig. 13B). Without any authigenic flux, the organic carbon burial must shift dynamically from an elevated baseline of $f_{\text{OC}} \approx 0.3$ (black line) to 0.4 at the peak of the Hangenberg CIE (*ca* 360 Ma). This prediction is compatible with the stratigraphic placement of the Hangenberg black shales below the Devonian–Carboniferous boundary (Fig. 1) and may have been achieved by increased organic matter preservation in anoxic basins ($\uparrow f_{\text{OC}}$) in tandem with decreased marine carbonate burial ($\downarrow f_{\text{MC}}$; see the section on *Geological context*; Fig. 2). The increased rate of organic carbon burial would be associated with a drawdown of CO_2 and release of O_2 , which is supported by proxy evidence and models for cooling climates and increasing pO_2 through the end-Devonian (Isaacson *et al.*, 2008; Berner, 2009; Kaiser *et al.*, 2016). Alternatively, the burial of isotopically offset authigenic carbonates may have contributed to enriching $\delta^{13}\text{C}_{\text{DIC}}$. Based on assumptions from Schrag *et al.* (2013), it would be reasonable to posit that authigenic carbonate burial could force the end-Devonian $\delta^{13}\text{C}_{\text{DIC}}$ trends with practically

no elevated f_{OC} (blue; Fig. 13). However, an empirical estimate of ε_{AC} from Bakken data (green; Fig. 13) shows that even tripling the fractional burial of authigenic carbonate cannot significantly enrich $\delta^{13}C_{DIC}$, and instead still requires an elevated f_{OC} to drive the CIE.

This is further illustrated when the $\delta^{13}C$ stack is inverted to calculate the necessary f_{AC} forcings for a constant f_{OC} of 0.2 to 0.3 (Fig. 13C). When ε_{AC} is assumed to be significant (17.5‰; blue), the baseline Late Devonian $\delta^{13}C_{DIC}$ values can be explained by a minor authigenic sink ($f_{AC} \leq 0.1$) increasing to 0.14 at the Hangenberg CIE. Conversely, adopting an ε_{AC} modelled after Bakken data (4‰; green), the authigenic burial rate must shift drastically to drive seawater isotopic evolution. The maxima and minima of the modelled f_{AC} range above 1.0 and below 0.0, reflecting the limitation of a model forced only by isotopically intermediate authigenic carbonate burial. Therefore, in contrast to model expectations, this study's data suggest that, despite the large volume of authigenic cements observed in the Bakken, their isotopic mass-balance contribution to the Hangenberg CIE must have been minor and secondary to organic carbon burial.

One additional carbon cycle forcing is the isotopic composition of riverine weathered carbon ($\delta^{13}C_W$; Kump *et al.*, 1999; Melchin & Holmden, 2006): $\delta^{13}C_W$ typically approximates mantle carbon composition (−5‰) at steady state, representing an admixture of weathered carbonate rock and fossil organic carbon. The authors (Kump *et al.*, 1999) proposed that during a major regression caused by the Hirnantian glaciation, broad swaths of shallow-water carbonate platforms were exposed to chemical weathering, driving $\delta^{13}C_W$ to more enriched values and contributing to a positive CIE in the Late Ordovician. The inverted Devonian–Carboniferous $\delta^{13}C_{DIC}$ record shows that this same forcing could feasibly account for the Hangenberg CIE (Fig. 13D): a shift of $\delta^{13}C_W$ from −4 to 0‰ would sufficiently enrich the $\delta^{13}C_{DIC}$ and is comparable to the proportion of limestone in the weathering flux ($f_{W,LS}$) increasing from ca 80 to 90%, assuming $\delta^{13}C_{carb} = +2.5$ ‰. The Hangenberg glaciation drove a global regression (Fig. 1), supporting this forcing hypothesis, and the continental bedrock exposed during the base-level fall was probably rich in carbonates based on Devonian lithostratigraphy (Fig. 2). Although unlikely, given the global evidence for increased organic carbon burial, an enrichment of $\delta^{13}C_W$ from weathered Devonian carbonates

could have driven the Hangenberg CIE without invoking any change to f_{OC} or f_{AC} .

With the present data, it is impossible to constrain the exact mechanism for the Hangenberg positive carbon-isotope excursion, but it seems likely that multiple factors were involved. The global occurrence of black shales and reduced reef deposits supports an organic carbon burial origin, but these siliciclastics also hosted a significant mass of isotopically intermediate authigenic carbonate if the Bakken data are representative of black shales. Additionally, due to the apparent global marine regression across the Devonian–Carboniferous boundary, $\delta^{13}C_W$ is unlikely to have remained constant. One final consideration is that the inverse model results represent conservative predictions because M_C was set to modern values. Some model estimates of DIC mass in the Devonian range up to 2.5× higher than the modern (Arvidson *et al.*, 2006), and as the exogenic carbon reservoir increases its isotopic composition becomes more resistant to change. In turn, fluctuations in f_{OC} , f_{AC} and $\delta^{13}C_W$ forcings must greatly increase to explain the same $\delta^{13}C_{DIC}$ excursion (Bartley & Kah, 2004). Each of these modelled forcings likely contributed to driving the Hangenberg excursion, and future work quantifying the mass of authigenic carbonate and continental weathering regime through the Devonian–Carboniferous will continue to elucidate their respective roles.

One final consideration is that the modelled scenarios presented above (Fig. 13) rely upon the assumption that authigenic sedimentation in the Bakken and similar contemporary epeiric seaways are sufficiently connected to the global ocean DIC pool to drive secular trends in $\delta^{13}C_{DIC}$. Firstly, the global carbon-isotopic excursion records are largely derived from preserved epeiric carbonates and exhibit a variety of magnitudes in different units (Kaiser *et al.*, 2016); even chemostratigraphic records within the same basin show significantly different Hangenberg $\delta^{13}C$ trends depending on margin proximity and depth (Qie *et al.*, 2015). The 'canonical' excursion record in Fig. 13A may therefore not be representative of seawater DIC from which the Bakken was deposited. Furthermore, the Williston Basin was located at the southernmost reach of the Western Canadian Sedimentary Basin and likely had restricted seawater circulation (Smith *et al.*, 1995; Smith & Bustin, 1998). Williston $\delta^{13}C_{DIC}$ composition and correspondingly the depositing carbonates could have conceivably evolved independent of global ocean

composition. Because of this, the above model represents an end-member scenario for end-Devonian authigenesis: if global sedimentation were to approximate patterns observed in the Bakken, how much leverage could authigenic carbonate burial exert over the global carbon reservoir? Even making these broad assumptions which were predicted to maximize carbonate authigenesis *sensu* Schrag *et al.* (2013), including abundant organic matter and basin anoxia–euxinia which can produce very negative $\delta^{13}\text{C}$ -cements (e.g. Stakes *et al.*, 1999; Peckmann *et al.*, 2001), the fact that the modelled parameters indicate that authigenic burial had only a minor influence on $\delta^{13}\text{C}_{\text{DIC}}$ trends (Fig. 13B and C) is significant.

An alternative reading of the results is that Hangenberg $\delta^{13}\text{C}_{\text{carb}}$ records which vary between and within basins are indicative of local processes driving isotopic heterogeneity or overwriting the primary record (Qie *et al.*, 2015). The evidence for widespread anoxia and eutrophication in concert with base-level shift suggests that anaerobic respiration of organic matter was globally significant, but its effects on the local seawater and sediments could vary widely. If these local effects occurred relatively synchronously during the deposition of the transgressive Hangenberg black shale and following regression, then the cumulative impact of low- $\delta^{13}\text{C}$ carbonate cementation could drive multiple basins to higher $\delta^{13}\text{C}_{\text{DIC}}$ and ultimately feed back into the global ocean. A second explanation for these trends would be that the limestone units measured for Hangenberg $\delta^{13}\text{C}$ trends across the world incorporated different amounts of authigenic carbonate and subsequently were overwritten to various degrees, attenuating the isotopic excursion signal. The controls on local authigenic processes and their impact at a global level remain poorly understood not only in the modern ocean, but also the end-Devonian. Future attempts to constrain authigenic carbonate burial at broad spatial scales and elucidate its relationship with $\delta^{13}\text{C}_{\text{DIC}}$ will continue to test the authigenic carbon model and allow for more meaningful interpretations of secular trends in seawater carbonate isotopic composition.

CONCLUSIONS

The authigenic carbonate revision of the global carbon cycle model (Schrag *et al.*, 2013) was based on observations made from modern sites of authigenesis and assumes that similar

processes would have been more prevalent during intervals with low pO_2 , a large dissolved inorganic carbon (DIC) reservoir and reduced biological pump (Higgins *et al.*, 2009). Ongoing efforts to measure carbonate authigenesis rates in sea floor sediments (Mitnick *et al.*, 2018; Bradbury & Turchyn, 2019) provide important constraints on modern f_{AC} , but represent an imperfect analogue for Palaeozoic sediments deposited in poorly oxygenated basins prior to the advent of pelagic calcification. Based on modern expectations, the Bakken black shales were deposited in conditions conducive to the formation of isotopically offset authigenic carbonates, but instead host large volumes of disseminated carbonates (7 to 9 wt.%) which are isotopically intermediate ($\epsilon_{\text{AC}} \approx 0.3\text{‰}$ to 3.7‰). Whereas initial model expectations predict that increased f_{AC} could independently drive the Hangenberg positive carbon-isotope excursions (CIE), the new empirical parameters suggest that authigenic carbonate burial represented a minor contribution to the seawater $\delta^{13}\text{C}_{\text{DIC}}$ shift. Given the disconnect between modern carbonate authigenesis and the mid-Palaeozoic data presented here, the critical question going forward becomes: *what processes control the burial of authigenic carbonate through Earth's history?*

The geochemical results presented herein suggest that the end-Devonian Williston Basin supported an active sulphate-reducing microbial (SRM) community which had abundant organic carbon to remineralize. However, the $\delta^{13}\text{C}_{\text{carb}}$ data indicate that the majority of carbonate was sourced from dissolved inorganic carbon rather than oxidized organic matter, in contrast with low- $\delta^{13}\text{C}$ authigenic cements from similar geological deposits (Stakes *et al.*, 1999). These findings are similar to other surveys of intermediate- $\delta^{13}\text{C}$ siliciclastic-hosted cements in the Cambrian (Gaines & Vorhies, 2016) and Late Permian (Saitoh *et al.*, 2015). On the basis of these commonalities, this study hypothesizes that conditions in the Palaeozoic which supported episodes of widespread carbonate authigenesis were fundamentally different from the modern ocean in that poorly-oxygenated basins facilitated anaerobic oxidation of organic carbon at or above the sediment–water interface, allowing authigenic precipitation adjacent to an augmented DIC reservoir and significant mixing with this isotopically enriched pool (Saitoh *et al.*, 2015). Different controls in the Precambrian may have yielded similar authigenic carbonates: isotopically enriched cements from the Proterozoic (Li *et al.*, 2015)

were interpreted to reflect limited oxidants (SO_4^{2-}) prohibiting organoclastic sulphate reduction, as well as $\delta^{13}\text{C}$ enrichment in the presence of methanogens. In summary, the conditions which enable global authigenic carbonate formation in the modern ocean seem to be unique, whereas controls on authigenesis in deep-time remain diverse and ambiguous. The bulk methods presented here can serve as a template for future efforts to quantify authigenic carbonates at a formation scale, and by doing so better understand their role in the global carbon cycle.

ACKNOWLEDGEMENTS

Drill core samples were made available courtesy of the USGS CRC. The authors thank L. Wingate at the University of Michigan Stable Isotope Laboratory and A. Schauer at the University of Washington Isolab for stable isotopic analyses. We are grateful to J. Zambito and the Wisconsin Geological & Natural History Survey for XRF analyses. We thank J. Valley, J. Zambito, A. Carroll and S. Meyers for helping to shape the research project, and M. Śliwiński, A. Denny, B. Linzmeier, S. McMullin, H. Cui and M. Patzkowsky for stimulating discussions about the results. The interpretation of these results was further supported by Śliwiński, M.G. *et al.*, unpublished data, which can be accessed at http://www.geology.wisc.edu/homepages/wiscsims/public_html/pdfs/Sliwinski_Unpub2019.pdf. This work was supported by the AAPG Robert and Carolyn Maby Memorial Grant and the GSA Alexander and Geraldine Wanek Award. The data that support the findings of this study are available through the USGS CRC at <https://my.usgs.gov/crcwc/core/report/11025> and <https://my.usgs.gov/crcwc/core/report/16324>. This manuscript benefitted from constructive reviews by S. B. Pruss, M. Wallace and B. Gill, as well as comments by Associate Editor N. Tosca.

CONFLICT OF INTEREST

The authors declare that they have no conflict of interests.

REFERENCES

- Aderoju, T.** and **Bend, S.** (2018) Reconstructing the palaeoecosystem and palaeodepositional environment within the Upper Devonian–Lower Mississippian Bakken Formation: a biomarker approach. *Org. Geochem.*, **119**, 91–100.
- Algeo, T.J.** and **Tribovillard, N.** (2009) Environmental analysis of paleoceanographic systems based on molybdenum–uranium covariation. *Chem. Geol.*, **268**, 211–225.
- Algeo, T.J., Lyons, T.W., Blakey, R.C.** and **Over, D.J.** (2007) Hydrographic conditions of the Devonian–Carboniferous North American Seaway inferred from sedimentary Mo–TOC relationships. *Palaeogeogr. Palaeoclimatol. Palaeoecol.*, **256**, 204–230.
- Allan, J.R.** and **Matthews, R.K.** (1982) Isotope signatures associated with early meteoric diagenesis. *Sedimentology*, **29**, 797–817.
- Aller, R.C.** and **Blair, N.E.** (2006) Carbon remineralization in the Amazon–Guianas tropical mobile mudbelt: a sedimentary incinerator. *Cont. Shelf Res.*, **26**, 2241–2259.
- Angulo, S.** and **Buatois, L.A.** (2012) Ichnology of a Late Devonian–Early Carboniferous low-energy seaway: the Bakken Formation of subsurface Saskatchewan, Canada: assessing paleoenvironmental controls and biotic responses. *Palaeogeogr. Palaeoclimatol. Palaeoecol.*, **315–316**, 46–60.
- Arp, G., Reimer, A.** and **Reitner, J.** (2001) Photosynthesis-induced biofilm calcification and calcium concentrations in Phanerozoic oceans. *Science*, **292**, 1701–1704.
- Arthur, M.A., Dean, W.E.** and **Schlanger, S.O.** (1985) Variations in the global carbon cycle during the cretaceous related to climate, volcanism, and changes in atmospheric CO_2 . In: *The Carbon Cycle and Atmospheric CO_2 : Natural Variations Archean to Present* (Eds E.T. Sundquist and W.S. Broecker), Am. Geophys. Union Monogr., **32**, 504–529.
- Arvidson, R.S., Mackenzie, F.T.** and **Guidry, M.W.** (2006) MAGIC: a comprehensive model for earth system geochemical cycling over Phanerozoic time. *Am. J. Sci.*, **306**, 135–190.
- Banner, J.L.** and **Hanson, G.N.** (1990) Calculation of simultaneous isotopic and trace element variations during water–rock interaction with applications to carbonate diagenesis. *Geochim. Cosmochim. Acta*, **54**, 3123–3137.
- Bartley, J.K.** and **Kah, L.C.** (2004) Marine carbon reservoir, $\text{C}_{\text{org}}\text{--}\text{C}_{\text{carb}}$ coupling, and the evolution of the Proterozoic carbon cycle. *Geology*, **32**, 129–132.
- Baud, A., Richoz, S.** and **Pruss, S.** (2007) The lower Triassic anachronistic carbonate facies in space and time. *Global Planet. Change*, **55**, 81–89.
- Becker, R.T., Kaiser, S.I.** and **Aretz, M.** (2016) Review of chrono-, litho- and biostratigraphy across the global Hangenberg Crisis and Devonian–Carboniferous boundary. In: *Devonian Climate, Sea Level and Evolutionary Events* (Eds R.T. Becker, P. Königshof and C.E. Brett), Geol. Soc. London Spec. Publ., **423**, 355–386.
- Bergmann, K.D., Grotzinger, J.P.** and **Fischer, W.W.** (2013) Biological influences on seafloor carbonate precipitation. *Palaios*, **28**, 99–115.
- Berner, R.A.** (1968) Calcium carbonate concretions formed by the decomposition of organic matter. *Science*, **159**, 195–197.
- Berner, R.A.** (1991) A model for atmospheric CO_2 over Phanerozoic time. *Am. J. Sci.*, **291**, 339–376.
- Berner, R.A.** (2003) The long-term carbon cycle, fossil fuels and atmospheric composition. *Nature*, **426**, 323–326.
- Berner, R.A.** (2009) Phanerozoic atmospheric oxygen: new results using the GEOCARBSULF model. *Am. J. Sci.*, **309**, 603–606.
- Blakey, R.** (2016) North American Paleogeography. Available at: www2.nau.edu/rcb7/. accessed February 2016.
- Bless, M.J.M., Becker, R.T., Higgs, K., Papproth, E.** and **Streel, M.** (1993) Eustatic cycles around the Devonian–Carboniferous boundary and the sedimentary and fossil

- record in Sauerland (Federal Republic of Germany). *Ann. Soc. Géol. Belg.*, **115**, 689–702.
- Boyer, D.L., Owens, J.D., Lyons, T.W. and Droser, M.L.** (2011) Joining forces: combined biological and geochemical proxies reveal a complex but refined high-resolution palaeo-oxygen history in Devonian epeiric seas. *Palaeogeogr. Palaeoclimatol. Palaeoecol.*, **306**, 134–146.
- Bradbury, H.J. and Turchyn, A.V.** (2019) Reevaluating the carbon sink due to sedimentary carbonate formation in modern marine sediments. *Earth Planet. Sci. Lett.*, **519**, 40–49.
- Brand, U. and Veizer, J.** (1980) Chemical diagenesis of a multicomponent carbonate system – 1: trace elements. *J. Sed. Res.*, **50**, 1219–1236.
- Brand, U., Legrand-Blain, M. and Streel, M.** (2004) Biochemostratigraphy of the Devonian-Carboniferous boundary global stratotype section and point, Griotte Formation, La Serre, Montagne Noire, France. *Palaeogeogr. Palaeoclimatol. Palaeoecol.*, **205**, 337–357.
- Brennan, S.W.** (2016) Integrated Characterization of Middle Bakken Diagenesis, Williston Basin, North Dakota, U.S.A. PhD Dissertation, Colorado School of Mines, Golden, CO, 137 pp.
- Brodie, M.W., Aplin, A.C., Hart, B., Orland, I.J., Valley, J.W. and Boyce, A.J.** (2018) Oxygen isotope microanalysis by secondary ion mass spectrometry suggests continuous 300-million-year history of calcite cementation and dolomitization in the Devonian Bakken Formation. *J. Sed. Res.*, **88**, 91–104.
- Broecker, W.S.** (1970) A boundary condition on the evolution of atmospheric oxygen. *J. Geophys. Res.*, **75**, 3553–3557.
- Buggisch, W. and Joachimski, M.M.** (2006) Carbon isotope stratigraphy of the Devonian of Central and Southern Europe. *Palaeogeogr. Palaeoclimatol. Palaeoecol.*, **240**, 68–88.
- Calvert, S.E. and Pedersen, T.F.** (2007) Elemental proxies for palaeoclimatic and palaeoceanographic variability in marine sediments: interpretation and application. In: *Proxies in Late Cenozoic Paleoceanography* (Eds C. Hillaire-Marcel and A. de Vernal), *Developments in Marine Geology*, **1**, 567–644.
- Caplan, M.L. and Bustin, R.M.** (1998) Palaeoceanographic controls on geochemical characteristics of organic-rich Exshaw mudrocks: role of enhanced primary production. *Org. Geochem.*, **30**, 161–188.
- Caplan, M.L. and Bustin, R.M.** (1999) Devonian-Carboniferous Hangenberg mass extinction event, widespread organic-rich mudrock and anoxia: causes and consequences. *Palaeogeogr. Palaeoclimatol. Palaeoecol.*, **148**, 187–207.
- Carmichael, S.K., Waters, J.A., Batchelor, C.J., Coleman, D.M., Suttner, T.J., Kido, E., Moore, L.M. and Chadimová, L.** (2016) Climate instability and tipping points in the Late Devonian: detection of the Hangenberg Event in an open oceanic island arc in the Central Asian Orogenic Belt. *Gondwana Res.*, **32**, 213–231.
- Coleman, M.L. and Raiswell, R.** (1993) Microbial mineralization of organic matter: mechanisms of self-organization and inferred rates of precipitation of diagenetic minerals. *Phil. Trans. Roy. Soc. London A Math. Phys. Eng. Sci.*, **344**, 69–87.
- Copper, P.** (1994) Ancient reef ecosystem expansion and collapse. *Coral Reefs*, **13**, 3–11.
- Cramer, B.D., Saltzman, M.R., Day, J.E. and Witzke, B.J.** (2008) Record of the Late Devonian Hangenberg global positive carbon-isotope excursion in an epeiric sea setting: carbonate production, organic-carbon burial and paleoceanography during the late Famennian. In: *Dynamics of Epeiric Seas* (Eds B.R. Pratt and C. Holmden), *Geol. Assoc. of Canada Spec. Paper*, **48**, 103–118.
- Curtis, C.D. and Coleman, M.L.** (1986) Controls on the precipitation of early diagenetic calcite, dolomite and siderite concretions in complex depositional sequences. In: *Roles of Organic Matter in Sediment Diagenesis* (Ed. D.C. Gautier), *SEPM Spec. Publ.*, **38**, 23–34.
- Denny, A.C., Orland, I.J. and Valley, J.W.** (2020) Regionally Correlated Oxygen and Carbon Isotope Zonation in Diagenetic Carbonates of the Bakken Formation. *Chem. Geol.*, **531**, 119327.
- Des Marais, D.J., Strauss, H., Summons, R.E. and Hayes, J.M.** (1992) Carbon isotope evidence for the stepwise oxidation of the Proterozoic environment. *Nature*, **359**, 605–609.
- Dickens, G.R.** (2003) Rethinking the global carbon cycle with a large, dynamic and microbially mediated gas hydrate capacitor. *Earth Planet. Sci. Lett.*, **213**, 169–183.
- Dyer, B., Maloof, A.C. and Higgins, J.A.** (2015) Glacioeustasy, meteoric diagenesis, and the carbon cycle during the Middle Carboniferous. *Geochem. Geophys. Geosyst.*, **16**, 3383–3399.
- Egenhoff, S.O.** (2017) The lost Devonian sequence – sequence stratigraphy of the middle Bakken member, and the importance of clastic dykes in the lower Bakken member shale, North Dakota, USA. *Mar. Petrol. Geol.*, **81**, 278–293.
- Egenhoff, S.O. and Fishman, N.S.** (2013) Traces in the dark-sedimentary processes and facies gradients in the upper shale member of the Upper Devonian-Lower Mississippian Bakken Formation, Williston Basin, North Dakota, U.S.A. *J. Sed. Res.*, **83**, 803–824.
- Egenhoff, S.O., van, Dolah, A., Jaffri, A. and Maletz, J.** (2011) Facies architecture and sequence stratigraphy of the Middle Bakken Member, Williston Basin, North Dakota. In: *The Bakken-Three Forks Petroleum System in the Williston Basin* (Eds J.W. Robinson, J.A. LeFever and S.B. Gaswirth), *Rocky Mountain Assoc. of Geol. Guidebook*, 27–47.
- Emrich, K., Ehhalt, D.H. and Vogel, J.C.** (1970) Carbon isotope fractionation during the precipitation of calcium carbonate. *Earth Planet. Sci. Lett.*, **8**, 363–371.
- Fishman, N.S., Egenhoff, S.O., Boehlke, A.R. and Lowers, H.A.** (2015) Petrology and diagenetic history of the upper shale member of the Late Devonian–Early Mississippian Bakken Formation, Williston Basin, North Dakota. In: *Paying Attention to Mudrocks: Priceless!* (Eds D. Larsen, S.O. Egenhoff and N.S. Fishman), *GSA Spec. Paper*, **515**, 125–151.
- Formolo, M.J., Lyons, T.W., Zhang, C., Kelley, C., Sassen, R., Horita, J. and Cole, D.R.** (2004) Quantifying carbon sources in the formation of authigenic carbonates at gas hydrate sites in the Gulf of Mexico. *Chem. Geol.*, **205**, 253–264.
- Formolo, M.J., Riedinger, N. and Gill, B.C.** (2014) Geochemical evidence for euxinia during the Late Devonian extinction events in the Michigan Basin (U.S.A.). *Palaeogeogr. Palaeoclimatol. Palaeoecol.*, **414**, 146–154.
- Gaines, R.R. and Vorhies, J.S.** (2016) Growth mechanisms and geochemistry of carbonate concretions from the Cambrian Wheeler Formation (Utah, USA). *Sedimentology*, **63**, 662–698.

- Garrels, R.M.** and **Lerman, A.** (1981) Phanerozoic cycles of sedimentary carbon and sulfur. *Proc. Natl Acad. Sci. USA*, **78**, 4652–4656.
- Gaswirth, S., Marra, K., Cook, T., Charpentier, R.R., Gautier, D.L., Higley, D.K., Klett, T.R., Lewan, M.D., Lillis, P.G., Schenk, C.J., Tennyson, M.E. and Whidden, K.J.** (2013) Assessment of Undiscovered Oil Resources in the Bakken and Three Forks Formations, Williston Basin Province, Montana, North Dakota, and South Dakota. *USGS Fact Sheet 2013–3013*, 4 pp.
- van Geldern, R., Joachimski, M.M., Day, J., Jansen, U., Alvarez, F., Yolkin, E.A. and Ma, X.P.** (2006) Carbon, oxygen and strontium isotope records of Devonian brachiopod shell calcite. *Palaeogeogr. Palaeoclimatol. Palaeoecol.*, **240**, 47–67.
- Grotzinger, J.P.** and **James, N.P.** (2000) Precambrian carbonates: evolution of understanding. In: *Carbonate Sedimentation and Diagenesis in the Evolving Precambrian World* (Eds J.P. Grotzinger and N.P. James), SEPM Special Publication, **67**, 3–20.
- Grotzinger, J.P.** and **Knoll, A.H.** (1995) Anomalous carbonate precipitates: is the Precambrian the key to the Permian? *Palaios*, **10**, 578–596.
- Hatch, J.R.** and **Leventhal, J.S.** (1992) Relationship between inferred redox potential of the depositional environment and geochemistry of the Upper Pennsylvanian (Missourian) Stark Shale Member of the Dennis Limestone, Wabaunsee County, Kansas, U.S.A. *Chem. Geol.*, **99**, 65–82.
- Hayes, J.M.** and **Waldbauer, J.R.** (2006) The carbon cycle and associated redox processes through time. *Phil. Trans. Roy. Soc. London B Biol. Sci.*, **361**, 931–950.
- Higgins, J.A., Fischer, W.W. and Schrag, D.P.** (2009) Oxygenation of the ocean and sediments: consequences for the seafloor carbonate factory. *Earth Planet. Sci. Lett.*, **284**, 25–33.
- Holland, H.D.** (1978) *The Chemistry of the Atmosphere and Oceans*. John Wiley and Sons, New York, 581 p.
- Isaacson, P.E., Díaz-Martínez, E., Grader, G.W., Kalvoda, J., Bábek, O. and Devuyt, F.X.** (2008) Late Devonian–earliest Mississippian glaciation in Gondwanaland and its biogeographic consequences. *Palaeogeogr. Palaeoclimatol. Palaeoecol.*, **268**, 126–142.
- Jiang, C., Li, M., Osadetz, K.G., Snowdon, L.R., Obermajer, M. and Fowler, M.G.** (2001) Bakken/Madison petroleum systems in the Canadian Williston Basin; Part 2: molecular markers diagnostic of Bakken and Lodgepole source rocks. *Org. Geochem.*, **32**, 1037–1054.
- Johnston, D.I., Henderson, C.M. and Schmidt, M.J.** (2010) Upper Devonian to Lower Mississippian conodont biostratigraphy of uppermost Wabamun Group and Palliser Formation to lowermost Banff and Lodgepole formations, southern Alberta and southeastern British Columbia, Canada: implications for correlations and sequence stratigraphy. *Bull. Can. Petrol. Geol.*, **58**, 295–341.
- Jones, B.** and **Manning, D.A.C.** (1994) Comparison of geochemical indices used for the interpretation of palaeoredox conditions in ancient mudstones. *Chem. Geol.*, **111**, 111–129.
- Kaiser, S.I., Becker, R.T., Spalletta, C. and Steuber, T.** (2009) High-resolution conodont stratigraphy, biofacies, and extinctions around the Hangenberg Event in pelagic successions from Austria, Italy, and France. *Palaeontol. Am.*, **63**, 97–139.
- Kaiser, S.I., Steuber, T., Becker, R.T. and Joachimski, M.M.** (2006) Geochemical evidence for major environmental change at the Devonian–Carboniferous boundary in the Carnic Alps and the Rhenish Massif. *Palaeogeogr. Palaeoclimatol. Palaeoecol.*, **240**, 146–160.
- Kaiser, S.I., Aretz, M. and Becker, R.T.** (2016) The global Hangenberg Crisis (Devonian–Carboniferous transition): review of a first-order mass extinction. In: *Devonian Climate, Sea Level and Evolutionary Events* (Eds R.T. Becker, P. Königshof and C.E. Brett), Geol. Soc. London Spec. Publ., **423**, 387–437.
- Karhu, J.A.** and **Holland, H.D.** (1996) Carbon isotopes and the rise of atmospheric oxygen. *Geology*, **24**, 867–870.
- Kiessling, W.** (2002) Secular variations in the Phanerozoic reef ecosystem. In: *Phanerozoic Reef Patterns* (Eds W. Kiessling, E. Flügel and J. Golanka), SEPM Spec. Publ., **72**, 625–690.
- Kozdon, R., Ushikubo, T., Kita, N.T., Spicuzza, M. and Valley, J.W.** (2009) Intratest oxygen isotope variability in the planktonic foraminifer *N. pachyderma*: real vs. apparent vital effects by ion microprobe. *Chem. Geol.*, **258**, 327–337.
- Kump, L.R.** and **Arthur, M.A.** (1999) Interpreting carbon-isotope excursions: carbonates and organic matter. *Chem. Geol.*, **161**, 181–198.
- Kump, L.R.** and **Garrels, R.M.** (1986) Modeling atmospheric O₂ in the global sedimentary redox cycle. *Am. J. Sci.*, **286**, 337–360.
- Kump, L.R., Arthur, M.A., Patzkowsky, M.E., Gibbs, M.T., Pinkus, D.S. and Sheehan, P.M.** (1999) A weathering hypothesis for glaciation at high atmospheric pCO₂ during the Late Ordovician. *Palaeogeogr. Palaeoclimatol. Palaeoecol.*, **152**, 173–187.
- Kump, L.R., Pavlov, A. and Arthur, M.A.** (2005) Massive release of hydrogen sulfide to the surface ocean and atmosphere during intervals of oceanic anoxia. *Geology*, **33**, 397–400.
- Kump, L.R., Junium, C., Arthur, M.A., Brasier, A., Fallick, A., Melezhik, V., Lepland, A., Crne, A.E. and Luo, G.** (2011) Isotopic evidence for massive oxidation of organic matter following the Great Oxidation Event. *Science*, **334**, 1694–1696.
- Kumpan, T., Bábek, O., Kalvoda, J., Grygar, T.M., Frýda, J., Becker, R.T. and Hartenfels, S.** (2015) Petrophysical and geochemical signature of the Hangenberg Events: an integrated stratigraphy of the Devonian–Carboniferous boundary interval in the Northern Rhenish Massif (Avalonia, Germany). *Bull. Geosci.*, **90**, 667–674.
- Kurtz, A.C., Kump, L.R., Arthur, M.A., Zachos, J.C. and Paytan, A.** (2003) Early Cenozoic decoupling of the global carbon and sulfur cycles. *Paleoceanography*, **18**, 1090.
- Lash, G.G.** (2018) Significance of stable carbon isotope trends in carbonate concretions formed in association with anaerobic oxidation of methane (AOM), Middle and Upper Devonian shale succession, western New York State, USA. *Mar. Petrol. Geol.*, **91**, 470–479.
- LeFever, J.A.** (2008) Bakken Formation map series. *North Dakota Geological Survey*, scale 1:1,000,000, 5 sheets.
- Lepland, A.** and **Stevens, R.L.** (1998) Manganese authigenesis in the Landsort Deep, Baltic Sea. *Mar. Geol.*, **151**, 1–25.
- Li, C., Planavsky, N.J., Love, G.D., Reinhard, C.T., Hardisty, D., Feng, L., Bates, S.M., Huang, J., Zhang, Q., Chu, X. and Lyons, T.W.** (2015) Marine redox conditions in the middle Proterozoic ocean and isotopic constraints on authigenic carbonate formation: insights from the Chuanlinggou Formation, Yanshan Basin, North China. *Geochim. Cosmochim. Acta*, **150**, 90–105.

- Lineback, J.A.** and **Davidson, M.L.** (1982) The Williston Basin – sediment-starved during the early Mississippian. In: *Fourth International Williston Basin Symposium* (Eds J.E. Christopher and K. Kaldi), Saskatchewan Geol. Soc. Spec. Publ., **6**, 1–6.
- Lohmann, K.C.** (1988) Geochemical patterns of meteoric diagenetic systems and their application to studies of paleokarst. In: *Paleokarst* (Eds N.P. James and P.W. Choquette), pp. 538–540. Springer, New York.
- Marynowski, L.** and **Filipiak, P.** (2007) Water column euxinia and wildfire evidence during deposition of the Upper Famennian Hangenberg event horizon from the Holy Cross Mountains (central Poland). *Geol. Mag.*, **144**, 569–595.
- Marynowski, L., Zatoń, M., Rakociński, M., Filipiak, P., Kurkiewicz, S.** and **Pearce, T.J.** (2012) Deciphering the upper Famennian Hangenberg Black Shale depositional environments based on multi-proxy record. *Palaeogeogr. Palaeoclimatol. Palaeoecol.*, **346**, 66–86.
- McGhee, G.R., Clapham, M.E., Sheehan, P.M., Bottjer, D.J.** and **Droser, M.L.** (2013) A new ecological-severity ranking of major Phanerozoic biodiversity crises. *Palaeogeogr. Palaeoclimatol. Palaeoecol.*, **370**, 260–270.
- Melchin, M.J.** and **Holmden, C.** (2006) Carbon isotope chemostratigraphy in Arctic Canada: sea-level forcing of carbonate platform weathering and implications for Hirnantian global correlation. *Palaeogeogr. Palaeoclimatol. Palaeoecol.*, **234**, 186–200.
- Mii, H.S., Grossman, E.L.** and **Yancey, T.E.** (1999) Carboniferous isotope stratigraphies of North America: implications for Carboniferous paleoceanography and Mississippian glaciation. *Geol. Soc. Am. Bull.*, **111**, 960–973.
- Mitnick, E.H., Lammers, L.N., Zhang, S., Zaretskiy, Y.** and **DePaolo, D.J.** (2018) Authigenic carbonate formation rates in marine sediments and implications for the marine $\delta^{13}\text{C}$ record. *Earth Planet. Sci. Lett.*, **495**, 135–145.
- Peckmann, J., Reimer, A., Luth, U., Luth, C., Hansen, B.T., Heinicke, C., Hoefs, J.** and **Reitner, J.** (2001) Methane-derived carbonates and authigenic pyrite from the northwestern Black Sea. *Mar. Geol.*, **177**, 129–150.
- Peters, S.E., Husson, J.M.** and **Czaplewski, J.J.** (2018) Macrostrat: a platform for geological data integration and deep-time Earth crust research. *Geochem. Geophys. Geosyst.*, **19**, 1393–1409.
- Pitman, J.K., Price, L.C.** and **LeFever, J.A.** (2001) Diagenesis and fracture development in the Bakken Formation, Williston Basin: implications for reservoir quality in the middle member. *US Geol. Surv. Prof. Pap.*, **1653**, 19.
- Playford, G.** and **McGregor, D.C.** (1993) Miospores and organic-walled microphytoplankton of Devonian–Carboniferous boundary beds (Bakken Formation), Southern Saskatchewan: a systematic and stratigraphic appraisal. *Bull. Geol. Surv. Can.*, **445**, 107.
- Price, L.C.** and **LeFever, J.A.** (1992) Does bakken horizontal drilling imply a huge oil-resource base in fractured shales? In: *Geological Studies Relevant to Horizontal Drilling: Examples from Western North America* (Eds J.W. Schmoker, E.B. Coalson and C.A. Brown), Rocky Mountain Assoc. of Geol. Guidebook, 199–214.
- Pruss, S.B., Bottjer, D.J., Corsetti, F.A.** and **Baud, A.** (2006) A global marine sedimentary response to the end-Permian mass extinction: examples from southern Turkey and the western United States. *Earth Sci. Rev.*, **78**, 193–206.
- Pruss, S.B., Corsetti, F.A.** and **Fischer, W.W.** (2008) Seafloor-precipitated carbonate fans in the Neoproterozoic Rainstorm Member, Johnnie Formation, Death Valley Region, USA. *Sed. Geol.*, **207**, 34–40.
- Qie, W., Liu, J., Chen, J., Wang, X., Mii, H., Zhang, X., Huang, X., Yao, L., Algeo, T.J.** and **Luo, G.** (2015) Local overprints on the global carbonate $\delta^{13}\text{C}$ signal in Devonian–Carboniferous boundary successions of South China. *Palaeogeogr. Palaeoclimatol. Palaeoecol.*, **418**, 290–303.
- Raiswell, R.** (1976) The microbiological formation of carbonate concretions in the Upper Lias of NE England. *Chem. Geol.*, **18**, 227–244.
- Raup, D.M.** and **Sepkoski, J.J.** (1982) Mass extinctions in the marine fossil record. *Science*, **215**, 1501–1503.
- Requejo, A.G., Allan, J., Creaney, S., Gray, N.R.** and **Cole, K.S.** (1992) Aryl isoprenoids and diaromatic carotenoids in Paleozoic source rocks and oils from the Western Canada and Williston Basins. *Org. Geochem.*, **19**, 245–264.
- Riding, R.** (2006) Microbial carbonate abundance compared with fluctuations in metazoan diversity over geological time. *Sed. Geol.*, **185**, 229–238.
- Riding, R.** (2009) An atmospheric stimulus for cyanobacterial-bioinduced calcification ca. 350 million years ago? *Palaios*, **24**, 685–696.
- Riding, R.** and **Liang, L.** (2005) Geobiology of microbial carbonates: metazoan and seawater saturation state influences on secular trends during the Phanerozoic. *Palaeogeogr. Palaeoclimatol. Palaeoecol.*, **219**, 101–115.
- Saitoh, M., Ueno, Y., Isozaki, Y., Shibuya, T., Yao, J., Ji, Z., Shozugawa, K., Matsuo, M.** and **Yoshida, N.** (2015) Authigenic carbonate precipitation at the end-Guadalupian (Middle Permian) in China: implications for the carbon cycle in ancient anoxic oceans. *Prog. Earth Planet. Sci.*, **2**, 41 pp.
- Saltzman, M.R.** and **Thomas, E.** (2012) Carbon isotope stratigraphy. In: *The Geologic Time Scale 2012* (Eds F.M. Gradstein, J.G. Ogg, M.D. Schmitz and G.M. Ogg), pp. 207–232. Elsevier, Amsterdam.
- Sandberg, P.A.** (1983) An oscillating trend in Phanerozoic non-skeletal carbonate mineralogy. *Nature*, **305**, 19–22.
- Schieber, J.** (2014) Traces in the dark—sedimentary processes and facies gradients in the Upper Devonian–Lower Mississippian Upper Shale Member of the Bakken Formation, Williston Basin, North Dakota, U.S.A. – discussion. *J. Sed. Res.*, **84**, 837–838.
- Schrag, D.P., Higgins, J.A., Macdonald, F.A.** and **Johnston, D.T.** (2013) Authigenic carbonate and the history of the global carbon cycle. *Science*, **339**, 540–543.
- Scott, C., Slack, J.F.** and **Kelley, K.D.** (2017) The hyper-enrichment of V and Zn in black shales of the Late Devonian–Early Mississippian Bakken Formation (USA). *Chem. Geol.*, **452**, 24–33.
- Shields, G.A.** and **Mills, B.J.W.** (2017) Tectonic controls on the long-term carbon isotope mass balance. *Proc. Natl Acad. Sci. USA*, **114**, 4318–4323.
- Smith, M.G.** and **Bustin, R.M.** (1996) Lithofacies and paleoenvironments of the Late Devonian and Early Mississippian Bakken Formation, Williston Basin. *Bull. Can. Petrol. Geol.*, **44**, 495–507.
- Smith, M.G.** and **Bustin, R.M.** (1998) Production and preservation of organic matter during deposition of the Bakken Formation (Late Devonian and Early Mississippian), Williston Basin. *Palaeogeogr. Palaeoclimatol. Palaeoecol.*, **142**, 185–200.
- Smith, M.G.** and **Bustin, R.M.** (2000) Late Devonian and Early Mississippian Bakken and Exshaw black shale

- source rocks, Western Canada Sedimentary Basin: a sequence stratigraphic interpretation. *AAPG Bull.*, **84**, 940–960.
- Smith, M.G., Bustin, R.M. and Caplan, M.L.** (1995) Sequence stratigraphy of the Bakken and Exshaw Formations: a continuum of black shale formations in the Western Canada Sedimentary Basin. In: *Seventh International Williston Basin Symposium* (Eds L.D.V. Hunter and R.A. Schalla), Montana Geol. Soc. Spec. Publ., 399–409.
- Stakes, D.S., Orange, D., Paduan, J.B., Salamy, K.A. and Maher, N.** (1999) Cold-seeps and authigenic carbonate formation in Monterey Bay, California. *Mar. Geol.*, **159**, 93–109.
- Summons, R.E. and Powell, T.G.** (1986) Chlorobiaceae in Palaeozoic seas revealed by biological markers, isotopes and geology. *Nature*, **319**, 763–765.
- Swart, P.K. and Oehlert, A.M.** (2018) Revised interpretations of stable C and O patterns in carbonate rocks resulting from meteoric diagenesis. *Sed. Geol.*, **364**, 14–23.
- Thrasher, L.C.** (1987) Macrofossils and stratigraphic subdivisions of the Bakken Formation (Devonian–Mississippian), Williston Basin, North Dakota. In: *Fifth International Williston Basin Symposium* (Eds C.G. Carlson and J.E. Christopher), Saskatchewan Geol. Soc. Spec. Publ., 53–67.
- Tribovillard, N., Algeo, T.J., Lyons, T. and Riboulleau, A.** (2006) Trace metals as paleoredox and paleoproductivity proxies: an update. *Chem. Geol.*, **232**, 12–32.
- USGS CRC (2016) USGS Core Research Center. Available at: <https://my.usgs.gov/crcwc/>. accessed 2016.
- Webb, G.E.** (1996) Was Phanerozoic reef history controlled by the distribution of non-enzymatically secreted reef carbonates (microbial carbonate and biologically induced cement)? *Sedimentology*, **43**, 947–971.
- Webb, G.E.** (2002) Latest Devonian and Early Carboniferous reefs: depressed reef building after the middle Paleozoic collapse. In: *Phanerozoic Reef Patterns* (Eds W. Kiessling, E. Flügel and J. Golanka), SEPM Spec. Publ., **72**, 239–269.
- Webster, R.L.** (1984) Petroleum source rocks and stratigraphy of the Bakken Formation in North Dakota. In: *Hydrocarbon Source Rocks of the Greater Rocky Mountain Region* (Eds J. Woodward, F.F. Meissner and J.C. Clayton), Rocky Mountain Assoc. Geol., 57–81.
- Wedepohl, K.H.** (1971) Environmental influences on the chemical composition of shales and clays. *Phys. Chem. Earth*, **8**, 307–333.
- Wilkinson, B.H. and Given, R.K.** (1986) Secular variation in abiogenic marine carbonates: constraints on Phanerozoic atmospheric carbon dioxide contents and oceanic Mg/Ca ratios. *J. Geol.*, **94**, 321–333.
- Woods, A.D. and Baud, A.** (2008) Anachronistic facies from a drowned Lower Triassic carbonate platform: lower member of the Alwa Formation (Ba'id Exotic), Oman Mountains. *Sed. Geol.*, **209**, 1–14.
- Yao, L., Aretz, M., Chen, J., Webb, G.E. and Wang, X.** (2016) Global microbial carbonate proliferation after the end-Devonian mass extinction: mainly controlled by demise of skeletal bioconstructors. *Sci. Rep.*, **6**, 1–9.
- Zambito, J.J., McLaughlin, P.I., Haas, L.D., Stewart, E.K., Bremner, S.E. and Hurth, M.J.** (2016) Sampling methodologies and data analysis techniques for geologic materials using portable x-ray fluorescence (pXRF) elemental analysis. *Wisconsin Geol. Nat. Hist. Surv. Open-File Rep.* 2016-02, 12 pp.
- Zhu, Z., Aller, R.C. and Mak, J.** (2002) Stable carbon isotope cycling in mobile coastal muds of Amapá, Brazil. *Cont. Shelf Res.*, **22**, 2065–2079.

Manuscript received 11 June 2019; revision accepted 29 November 2019

Supporting Information

Additional information may be found in the online version of this article:

Table S1. Bulk rock elemental abundance data from Bakken core samples measured by hand-held X-ray fluorescence (HHXRF).